Supplement of

Surprisingly Robust Photochemistry in Subarctic Particles During Winter: Evidence from Photooxidants

Laura M. D. Heinlein[1], Junwei He[1], Michael Oluwatoyin Sunday[1*], Fangzhou Guo[2**], James Campbell[3], Allison Moon[4], Sukriti Kapur[5], Ting Fang[5***], Kasey Edwards[5], Meeta Cesler-Maloney[3****], Alyssa J. Burns[1], Jack Dibb[6], William Simpson[3], Manabu Shiraiwa[5], Becky Alexander[4], Jingqiu Mao[3], James H. Flynn III[2], Jochen Stutz[7], Cort Anastasio[1]

[1]Department of Land, Air and Water Resources, University of California, Davis, California 95616, USA
[2]Department of Earth & Atmospheric Sciences, University of Houston, Houston, TX 77204, USA
[3]Department of Chemistry and Biochemistry, University of Alaska, Fairbanks, Alaska 99775, USA
[4]Department of Atmospheric Sciences, University of Washington, Seattle, WA 98195, USA
[5]Department of Chemistry, University of California, Irvine, CA 92697, USA
[6]College of Engineering & Physical Sciences, University of New Hampshire, Durham, NH 03824, USA
[7]Department of Atmospheric & Oceanic Sciences, University of California, Los Angeles, CA 90095, USA

* Now at: California Air Resources Board, Sacramento, CA, USA
** Now at: Center for Atmospheric and Environmental Chemistry, Aerodyne Research Inc, Billerica, Massachusetts 01821, USA
*** Now at: Sustainable Energy and Environment Thrust, The Hong Kong University of Science and Technology (Guangzhou), Guangzhou, Guangdong 511400, China
**** Now at: Louisville Metro Air Pollution Control District, Louisville, Kentucky 40203, USA

Correspondence to: Cort Anastasio (canastasio@ucdavis.edu)

Submitted to Atmospheric Chemistry and Physics on February 20th, 2025.

Table of Contents

90

Section S1. Sample collection and storage

At the CTC site, $PM_{2.5}$ filter samples were collected with a 4-stage cascade impactor using quartz filters (TE-QMA and TE-230-QZ). Prior to sample collection, the filters were rinsed with 18 MΩ-cm water, baked at 500 ℃ for 8 hours, wrapped in aluminum foil, and stored in airtight polyethylene bags. At the House site, filter samples were collected on quartz microfiber
95 filters (Pallflex Emfab). The filters were precleaned by gently shaking in Milli-Q water for 4 hours, dried at 100 ℃, baked at 550 ℃ for 5 hours, stored in aluminum foil (treated by baking at 550 ℃ for 12 hours), and placed in airtight polyethylene bags until sample collection. After sample collection, filters were again wrapped in aluminum foil, placed in air-tight polyethylene bags, transported over ice in coolers, and then stored in a -20 ℃ freezer. Because filters were shared among several groups, ¼ of each filter was cut off at UC Irvine or the University of Washington, wrapped in aluminum foil, placed
100 in air-tight polyethylene bags, and shipped to UC Davis in a cooler over ice. The quarter filters were then stored at Davis in a -20 ℃ freezer until extraction.

Section S2. Screening factor calculation

In the solar simulator, as light passes through the 1 mL reaction tube and is absorbed by the solution, the photon flux decreases (Smith et al., 2016). To account for this attenuation of light though the reaction tube, we calculated the screening
105 factor (S_λ) for each extract:

$$S_\lambda = \frac{\sum[(1 - 10^{-A_\lambda}) \times I_\lambda]}{\sum[(2.303 \times A_\lambda) \times I_\lambda]} \tag{S1}$$

where A_λ is the absorbance of the particulate matter extract at wavelength λ (unitless) and I_λ is the photon flux of the solar simulator at wavelength λ (Smith et al., 2016). The measured pseudo-first order decay rates of probes are then corrected for screening using equation 2.

110 **Section S3.** Rate of light absorbance calculation

The rate of light absorbance in a PM extract in the solar simulator was calculated with

$$R_{abs,EXP,PME} = \frac{[DOC]_{PME}}{10^3} \times \sum_{300\,nm}^{550\,nm} (MAC_\lambda \times I_{\lambda,EXP} \times \Delta\lambda) \tag{S2}$$

where [DOC]$_{PME}$ is the dissolved organic carbon concentration in the extract (mg L^{-1}), the 10^3 factor is a unit conversion of mg to g, MAC$_\lambda$ is the DOC-normalized mass absorption cross section at wavelength λ (cm^2 g^{-1}), $I_{\lambda,EXP}$ is the surface-area-normalized photon flux at wavelength λ in the illuminated quartz tube (mol-photons cm^{-2} nm^{-1} s^{-1}), and $\Delta\lambda$ is the wavelength interval between discreet I_λ values (nm) (Kaur et al., 2019). In our simulated sunlight illumination system, we determined $I_{\lambda,EXP}$ as described in Hullar et al. (2020). Note that this $R_{abs,EXP,PME}$ only accounts for the light absorbed by water-soluble species that were extracted from the PM$_{2.5}$ filters into our extracts. Water-insoluble BrC, which also absorbs light and produces photooxidants, is not included in our water extracts.

Section S4. Experimental kinetic calculation: oxidant concentrations and oxidant production rates

All rates of light absorbance, photooxidant concentrations, and photooxidant production rates in this paper are reported under two actinic flux conditions: (1) at j_{2NB} = 0.0045 s^{-1}, the photolysis frequency of 2-nitrobenzaldehyde for Fairbanks midday actinic flux on February 1st, 2022 determined using actinic sunlight modeled by Tropospheric Ultraviolet and Visible (TUV) Radiation (Madronich and Flocke, 1998), or (2) at the photon flux condition determined for each specific composite period (Section 2.6.1).

Hydroxyl Radical

The $^\bullet$OH steady-state concentrations under laboratory conditions were measured using a low concentration (10 μM) of the probe benzoic acid (BA) (Anastasio and McGregor, 2001; Kaur et al., 2019; Ma et al., 2024). $^\bullet$OH concentrations were determined for each sample by simultaneously monitoring the loss of BA and the production of para-hydroxybenzoic acid (*p*-HBA) (Ma et al., 2022, 2023, 2024). The loss of BA was fit and normalized to a standard photon flux using equations 1 and 2 to determine the first-order rate constant for BA loss, $k'_{BA,EXP}$. The experimental $^\bullet$OH concentration in our PM extract (PME) was determined with

$$[\bullet OH]_{EXP,PME} = \frac{k'_{BA,EXP}}{k_{\bullet OH+BA}} \tag{S3}$$

where $k_{\bullet OH+BA}$ is the second-order rate constant for the reaction of $^\bullet$OH with BA at the pH of the extract, determined based on the rate constants for $^\bullet$OH with benzoic acid and benzoate (4.3×10^9 M^{-1} s^{-1} for benzoic acid, Ashton et al., 1995; Wander et al., 1968; 5.9×10^9 M^{-1} s^{-1} for benzoate, Ross et al., 1994) and the mole fractions of neutral and deprotonated benzoic acid (pK_a = 4.2; Wander et al., 1968). The production of *p*-HBA was fit using

$$[p - HBA]_t = [p - HBA]_0 + A(1 - e^{-Bt}) \tag{S4}$$

where $[p\text{-HBA}]_0$ is the initial concentration, $[p\text{-HBA}]_t$ is the concentration at time t, and A and B are fitted parameters (Ma et al., 2023, 2024). The product of A and B is the initial rate of p-HBA production ($R_{p\text{-HBA,EXP}}$), which is used to calculate the steady-state $^\bullet$OH concentration:

$$[\bullet\text{OH}]_{\text{EXP,PME}} = \frac{R_{p-\text{HBA,EXP}}}{[\text{BA}]_0 \times k_{\bullet\text{OH+BA}} \times Y_{p-\text{HBA}}} \tag{S5}$$

where $[\text{BA}]_0$ is the initial BA concentration and $Y_{p\text{-HBA}}$ is the yield of p-HBA from the reaction of $^\bullet$OH and BA (17%) (Anastasio and McGregor, 2001). The reported $^\bullet$OH concentration for a given extract is the average of the values determined by BA loss and p-HBA production. The average ($\pm 1\sigma$) relative percent difference in $^\bullet$OH concentration determined for the two methods is 18($\pm$51)%.

The steady-state $^\bullet$OH concentration was used to estimate the production rate of $^\bullet$OH in each extract with

$$P_{\bullet\text{OH,EXP,PME}} = [\bullet\text{OH}]_{\text{EXP,PME}} \times k_{\bullet\text{OH+DOC}} \times [\text{DOC}]_{\text{PME}} \tag{S6}$$

where $k_{\bullet\text{OH+DOC}}$ is the general second-order rate constant for reaction of $^\bullet$OH with atmospheric DOC, $3.8(\pm 1.9) \times 10^8$ L mol-C^{-1} s^{-1} (Arakaki et al., 2013). This assumes that DOC is the dominant $^\bullet$OH sink (Ma et al., 2023), which should be true for our DOC-rich extracts.

Singlet Molecular Oxygen

Steady-state $^1\text{O}_2^*$ concentrations were measured using a low concentration (10 μM) of the probe furfuryl alcohol (FFA) (Anastasio and McGregor, 2001; Appiani et al., 2017; Bogler et al., 2022; Kaur et al., 2019; Ma et al., 2024). Initially, we used the D$_2$O diagnostic method to measure $^1\text{O}_2^*$. With this technique, two parallel experiments were performed: PM extracts were diluted 2-fold with either Milli-Q H$_2$O or D$_2$O, which varies the rate constant for $^1\text{O}_2^*$ quenching by the solvent (Ma et al., 2023). While this technique has been successfully used to quantify $^1\text{O}_2^*$ in the past under more moderate pH conditions (Anastasio and McGregor, 2001; Haag and Hoigne, 1986; Ma et al., 2023), in our pH 1 extracts the D$_2$O method systematically underestimated $[^1\text{O}_2^*]$ compared to the result determined measuring FFA loss in Milli-Q (with correction for the loss of FFA due to $^\bullet$OH). Thus we measured FFA decay in our pH 1 extract without D$_2$O, assuming the dominant loss of $^1\text{O}_2^*$ was to the solvent H$_2$O. The normalized pseudo-first-order rate constant for FFA loss (k'_{FFA}) was determined using equations 2 and 3. We corrected for FFA loss due to $^\bullet$OH in order to determine the rate constant for FFA loss due to $^1\text{O}_2^*$ using

$$k'_{\text{FFA},1\text{O}2*} = k'_{\text{FFA}} - k_{\bullet\text{OH+FFA}} \times [\bullet\text{OH}]_{\text{EXP,PME}} \tag{S7}$$

where $k_{\bullet OH+FFA}$ is the second-order rate constant for FFA loss due to $^\bullet OH$, 1.5×10^{10} M^{-1} s^{-1} (Ross and Ross, 1977). The steady-state $^1O_2^*$ concentrations were then calculated using an equation analogous to equation S3, with the denominator being the second-order rate constant for FFA reacting with $^1O_2^*$ (at 10 °C, k_{1O2^*+FFA} is 8.06×10^7 M^{-1} s^{-1}; Appiani et al., 2017). The production rate of $^1O_2^*$ was predicted with an equation similar to equation S6, assuming that in the dilute particle extracts $^1O_2^*$ loss was mainly due to quenching by H_2O ($k'_{1O2^*,H2O} = 2.76(\pm0.02)\times10^5$ s^{-1}), with minor loss due to $^1O_2^*$ reacting with DOC ($k_{1O2^*+DOC} = 1\times10^5$ M^{-1} s^{-1}) (Appiani et al., 2017; Ma et al., 2023). In the dilute extracts, this is a reasonable assumption because H_2O and DOC are the two dominant $^1O_2^*$ sinks (Ma et al., 2023).

Triplet Excited States

The steady-state concentration of $^3C^*$ was determined using a low concentration (10 µM) of the probe syringol (SYR), which reacts with the subset of the triplet population that is oxidizing (Ma et al., 2022, 2023). A limitation to the SYR probe is that after SYR reacts with $^3C^*$, the oxidized syringyl phenoxyl radical can be reduced by other phenols or dissolved copper in solution to regenerate the parent SYR probe (Ma et al., 2022). This regeneration inhibits SYR loss and leads to an underestimate of $^3C^*$ concentrations (Ma et al., 2022, 2023; Wenk and Canonica, 2012). To account for probe regeneration, we measured the inhibition factor ($IF_{SYR,corr}$), which quantifies the fraction of $^3C^*$ and SYR reactions that lead to SYR loss (Section S5). Additionally, because SYR reacts with $^\bullet OH$ and $^1O_2^*$, we correct k'_{SYR} for SYR loss due to reactions with $^\bullet OH$ and $^1O_2^*$. Accounting for all corrections, the steady state $^3C^*$ concentration was then determined by

$$[^3C^*]_{EXP,PME} = \frac{k'_{SYR,EXP} - k_{SYR+\bullet OH} \times [\bullet OH]_{EXP,PME} - k_{SYR+1O2^*} \times [^1O_2^*]_{EXP,PME}}{k_{SYR+3C^*} \times IF_{SYR,corr}} \tag{S8}$$

where $k_{SYR+\bullet OH}$ and $k_{SYR+1O2^*}$ are the second-order rate constants for loss of SYR due to reaction with $^\bullet OH$ and $^1O_2^*$, respectively (Ma et al., 2022). Finally, the $^3C^*$ production rate in extracts was estimated using an equation analogous to equation S6, calculated using reactions of triplets with dissolved O_2 as the dominant sink ($k_{3C^*+O2} = 2.8\times10^9$ M^{-1} s^{-1}) and with DOC as a minor sink ($k_{3C^*+DOC,SYR} = 7\times10^7$ M^{-1} s^{-1}) (Kaur et al., 2019; Ma et al., 2023). In the dilute extracts, this is a reasonable assumption because other $^3C^*$ sinks, such as S(IV), are expected to be negligible in our PM extracts (Ma et al., 2023).

Section S5. Inhibition factor (Ma et al., 2022)

DOC in dilute particle extract can artificially suppress $[^3C^*]_{EXP,PME}$. When $^3C^*$ react with SYR, the product is a phenoxy radical, which can abstract a hydrogen from DOC to reform SYR, causing an artificial suppression in SYR loss. However, because DOC is a $^3C^*$ sink, DOC also causes a real suppression in $[^3C^*]_{EXP,PME}$ concentration and thus a smaller observed k'_{SYR}. We measure two inhibition factors to account for both types of inhibition by DOC.

The first inhibition factor we measured is the inhibition of the SYR probe (IF_{SYR}) which represents both inhibition due to quenching by DOC and inhibition due to the regeneration of the SYR probe. To measure IF_{SYR}, we performed three separate experiments. First, we spike 1 mL of a dilute extract with 10 µM SYR and measure the pseudo-first order decay of SYR ($k'_{SYR+PME}$). Next, we spike 1 mL of the dilute extract with 10 µM SYR and 80 µM of 3,4-dimethoxybenzaldehyde (DMB), a photosensitizer that produces $^3C^*$ ($k'_{SYR+DMB+PME}$). Lastly, we spike 1 mL of sulfuric acid (either pH 1 or pH 5, depending on pH of the extract we are testing) with 10 µM SYR and 80 µM DMB and measured the decay of SYR over time ($k'_{SYR+DMB}$). We then calculate IF_{SYR} by

$$IF_{SYR} = \frac{k'_{SYR+PME+DMB} - k'_{SYR+PME}}{k'_{SYR+DMB}}. \tag{S9}$$

DMB produces $^3C^*$, which react with SYR and lead to enhanced SYR loss, so we expect $k'_{SYR+DMB+PME}$ to be larger than $k'_{SYR+PME}$. If no inhibition occurs, $k'_{SYR+DMB}$ will be equivalent to the sum of $k'_{SYR+DMB+PME}$ and $k'_{SYR+PME}$ and IF_{SYR} will be 1. However, if either type of inhibition occurs, IF_{SYR} will be less than 1. Because IF_{SYR} accounts for both types of inhibition, but the $[^3C^*]_{EXP,PME}$ must only be corrected for the inhibition caused by regeneration of the SYR probe, we measure a second inhibition factor which only accounts for inhibition due to quenching of $^3C^*$ by DOC.

The second inhibition factor we measure is the inhibition of the probe FFA (IF_{FFA}). Analogous to IF_{SYR}, IF_{FFA} is measured by performing three experiments. First, we spike 1 mL of a dilute extract with 10 µM FFA and measure the decay of FFA over the illumination period ($k'_{FFA+PME}$). Next, we spike 1 mL of the dilute extract with 10 µM FFA and 80 µM of 3,4-dimethoxybenzaldehyde (DMB) ($k'_{FFA+DMB+PME}$). Lastly, we spike 1 mL of sulfuric acid (either pH 1 or pH 5) with 10 µM FFA and 80 µM DMB and measure the decay of FFA over time ($k'_{FFA+DMB}$). We then calculate IF_{FFA} with an equation analogous to equation S9. Finally, we correct IF_{SYR} by IF_{FFA} using

$$IF_{SYR,corr} = \frac{IF_{SYR}}{IF_{FFA}} \tag{S10}$$

where $IF_{SYR,corr}$ only accounts for the inhibition caused by the regeneration of the SYR probe.

Section S6. Calculating the concentration of dissolved organic carbon in aerosol liquid water

The DOC concentration in ALW was calculated using the flow rate of filter collection and the DOC measured in our PM extracts. First, the volume of air collected (m^3) per filter composite was calculated with

$$V_{air} = \sum_1^n \frac{Q \times t \times A_{extract}}{A_{total}} \tag{S11}$$

where n is the number of filters in each composite, Q is the flow rate reported for each filter (m^3 s^{-1}; Edwards et al., 2024; Moon et al., 2024), t is the collection time for each filter (s), A_{extract} is the area from each filter that was used to prepare the extract (cm^2), and A_{total} is the total area of a complete (i.e., uncut) filter (cm^2). V_{air} is calculated by adding up the volume of air sampled across the n filters used to make a given composite.

Next, the DOC concentration in ALW (mol-C L-aq^{-1}) was calculated with

$$[\text{DOC}]_{\text{ALW}} = \frac{[\text{DOC}]_{\text{PME}} \times V_{\text{aq}}}{V_{\text{air}} \times \text{ALWC}} \qquad (S12)$$

where $[\text{DOC}]_{\text{PME}}$ is the concentration of dissolved organic carbon measured in our PM filter extracts (mol-C L^{-1}), V_{aq} is the total volume of solution used to extract the filters in a composite (L), and ALWC is the aerosol liquid water content reported by Campbell et al. (2024) averaged over each composite (L-aq L-air^{-1}). Finally, the concentration factor (CF) between ALW conditions and our PM extracts was determined using

$$CF = \frac{[\text{DOC}]_{\text{ALW}}}{[\text{DOC}]_{\text{PME}}} \qquad (S13)$$

Values are reported in Table S12. The CF was used to extrapolate values measured in our dilute extracts (e.g., PM-mass/H$_2$O-mass ratios and P_{ox}) to ALW conditions.

Section S7. Estimating the inorganic S(IV) activities and activity coefficients

I. Calculating the Inorganic S(IV) Activity

A large uncertainty in our model of S(IV) oxidation pathways is the activity of inorganic S(IV). Measured S(IV) in the particles was categorized based on its susceptibility to oxidation by HOOH: total S(IV) measured by ion chromatography in filter extracts was considered the sum of inorganic S(IV) and hydroxymethanesulfonate (HMS), while HMS was determined as the S(IV) measured after hydrogen peroxide was added to the extracts to remove inorganic S(IV) (Dingilian et al., 2024). The difference of these two measurements should be the inorganic S(IV) amount. However, measured inorganic S(IV) concentrations in ALW (0.1–0.7 M, Dingilian et al., 2024) were roughly three orders of magnitude larger than predicted from Henry's law partitioning of SO$_2$ (corrected for temperature and ionic strength) assuming the ALW is pH 5 (resulting in 0.02-0.3 mM inorganic S(IV)) and six orders of magnitude higher assuming pH 1 ALW (0.02-0.2 µM).

To constrain the modeled particulate inorganic S(IV), we modeled the rate of secondary SO$_4^{2-}$ formation as a function of inorganic S(IV) activity (Figure 8a-d). We then defined the model estimate of inorganic S(IV) activity as the point where the

modeled fraction of secondary sulfate from HOOH – the dominant secondary sulfate source (Sunday et al., 2024) – matched
245   the fraction measured by sulfate isotope measurements (Moon et al., 2024). Under the high-NO_x conditions in Fairbanks, gas-phase HOOH concentrations are expected to be low (Ye et al., 2018). Sunday et al. (2024) describe that in-particle photochemistry is the main source of HOOH, with HOOH likely photochemically formed by $^3C^*$ reactions with phenols (Anastasio et al., 1997; Sunday et al., 2024). Our model uses the in-particle formation rates of sulfate reported by Sunday et al. (2024). Under the high-SO_2 conditions of ALPACA, HOOH is a unique condensed-phase oxidant because its rate of
250   SO_4^{2-} production is independent of {inorganic S(IV)}, a consequence of S(IV) being by far the most important sink for particle-phase HOOH (Sunday et al., 2024). In contrast, the other condensed-phase SO_4^{2-} formation pathways studied here become slower as {inorganic S(IV)} decreases. This property of the HOOH pathway allowed us to estimate the inorganic S(IV) activity.

II. Calculating the Inorganic S(IV) Activity Coefficient

255   We estimated the activity coefficient of inorganic S(IV) using the ionic-strength correction to Henry's Law for SO_2 described in Millero et al. (1989). The activity coefficient for inorganic S(IV) was estimated using

$$\gamma_{I_s} = \frac{H_{SO_2}}{H_{SO_2}^{I_s=0}} \tag{S14}$$

where $H_{SO_2}^{I_s=0}$ is temperature-adjusted Henry's Law constant for SO_2, determined with

$$H_{SO_2}^{I_s=0} = 1.23 \times e^{\left(3145.3 \times \left(\frac{1}{T} - \frac{1}{298}\right)\right)} \tag{S15}$$

260   (Seinfeld and Pandis, 2016) and H_{SO_2} is the Henry's Law constant for SO_2 at the same temperature but a non-zero ionic strength, determined with

$$log_{10}\left(\frac{H_{SO_2}}{H_{SO_2}^{I_s=0}}\right) = \left(\frac{22.3}{T} - 0.0997\right) \times I_s \quad (I_{s,max} = 6 \text{ M}) \tag{S16}$$

(Millero et al., 1989). While the ionic strength correction has been tested for $I_s \leq 6$ M, we use it for all our ALW calculations, where I_s values are as high as 23 M, due to of a lack of alternatives. The range of activity coefficients for aqueous SO_2
265   calculated in this work were 0.69-0.82 (Table S20).

Section S8. Isotopic signature of sulfate formed by $^3C^*$

We expect the dominant mechanism of SO_4^{2-} formation by $^3C^*$ to be either electron transfer or proton-coupled electron transfer from inorganic S(IV) to the oxidizing triplet excited state (McNeill and Canonica, 2016; Moon et al., 2024; Wang et al., 2020). The resulting isotopic signature of SO_4^{2-} formed by $^3C^*$ is equivalent to that of SO_4^{2-} formed from transition metal ions (TMI) (Moon et al., 2024). This indicates that the secondary SO_4^{2-} formed by TMI reported by Moon et al. (2024) represents the SO_4^{2-} formed by both $^3C^*$ and TMI.

Section S9. Determination of monthly photolysis frequencies for O_3, HONO, and BrC

Rate constants for photolysis of HONO and O_3 (i.e., $j_{HONO \to \cdot OH}$ and $j_{O3 \to O(1D)}$) on the 15th of each month were determined with TUV using constant column O_3 and aerosol optical depth (AOD), and with albedo estimated using ALPACA measurements (Table S22). Values of $j_{O3 \to O(1D)}$ were converted to $j_{O3 \to \cdot OH}$ by estimating the fraction of $O(^1D)$ lost due to reaction with H_2O (Table S23). First, we assumed the dominant loss pathways of $O(^1D)$ were H_2O, N_2, and O_2 (Seinfeld & Pandis, 2016). The H_2O gas concentration was determined using the monthly average relative humidity reported by the US Climate Research Network and temperatures reported by the Alaska Department of Transportation, both listed on the NOAA Environmental Research Division's Data Access Program Website (AK Fairbanks 11 NE, 2024). We calculated the temperature-dependent saturation vapor pressure for water as described in Seinfeld and Pandis (2016). The concentration of water was estimated by multiplying the saturation vapor pressure by the relative humidity. The temperature-dependent total concentration of gas molecules (i.e., Loschmidt's constant) was calculated using the ideal gas law and used to convert the concentration of H_2O to mlc cm^{-3}. We assume N_2 and O_2 were 78.8% and 20.95% of the total gas concentration, respectively. The pseudo-first order rate constants for $O(^1D)$ loss due to reaction with H_2O, N_2 and O_2 were then calculated using the respective temperature-corrected second-order rate constants (Seinfeld & Pandis, 2016). Using the pseudo-first order loss rate constants, the fraction of $O(^1D)$ loss due to reaction with H_2O ($f_{O(1D),H2O}$) was determined with

$$f_{O(1D),H2O} = \frac{k'_{O(1D),H2O}}{k'_{O(1D),H2O} + k'_{O(1D),N2} + k'_{O(1D),O2}} \tag{S17}$$

where each $k'_{O(1D)}$ term represents the pseudo-first order rate constant for $O(^1D)$ loss due to H_2O, N_2 and O_2. Finally, the rate of $^\bullet OH$ formation from ozone photolysis, $P_{O3 \to \cdot OH}$, was calculated by multiplying $P_{O3 \to O(1D)}$ with the fraction of $O(^1D)$ loss due to reaction with H_2O

$$P_{O3 \to \cdot OH} = P_{O3 \to O(1D)} \times f_{O(1D),H2O} \times 2 \tag{S18}$$

where the factor of two accounts for the molar ratio of two $^\bullet OH$ produced per $O(^1D)$ lost to reaction with water vapor. The value of $j_{O3 \to \cdot OH}$ was then determined by dividing $P_{O3 \to \cdot OH}$ by the O_3 concentration.

Rate constants for formation of oxidizing triplets following light absorption by brown carbon ($j_{BrC \rightarrow 3C*}$) were determined using TUV-modelled I_λ, the average MAC_λ determined from all House site samples, and the average Φ_{3C*} (2.7%) determined in this work. Values were determined for the wavelength range of 300 to 550 nm. TUV overestimates low-energy wavelengths in the winter in Fairbank (Figure S2a), leading to a 3-fold overestimate of $j_{O3 \rightarrow O(1D)}$ in winter (Figure S2b). This overestimate has minimal impact on $j_{HONO \rightarrow \bullet OH}$ or $j_{BrC \rightarrow 3C*}$ because these chromophores absorb most strongly at wavelengths greater than 325 nm (Figure S2c).

Section S10. Determination of monthly average concentrations of O_3, HONO, and BrC

Monthly average O_3 concentrations were determined by averaging the daily maximum 8-hour average O_3 reported by the Alaska DEC (Air Quality Monitoring Data, 2024), making the O_3 concentrations upper-bound estimates. HONO concentrations were estimated by first assuming the HONO-to-NO_2 ratio of 2.02($\pm$0.05)% measured during ALPACA applies year-round (Kuhn et al., in preparation; Simpson et al., 2024). Next, the monthly NO_2 concentration was determined by averaging the daily peak 1-hour NO_2 concentrations reported by ADEC (Air Quality Monitoring Data, 2024), making the HONO concentration an upper-bound estimate. We do not account for changes in HONO sources throughout the year, which likely changes the HONO-to-NO_2 ratio, but our estimate provides a reasonable upper-bound estimate of HONO (Kim et al., 2014).

For estimating particulate brown carbon concentrations, we first calculated the monthly average $PM_{2.5}$ concentration at the CTC site using daily average $PM_{2.5}$ concentrations reported by AKDEC (Air Quality Monitoring Data, 2024). Next, we assumed 52% of the total $PM_{2.5}$ is OA, the annual average OA-to-$PM_{2.5}$ fraction for Fairbanks reported by Kotchenruther (2016). This results in OA concentrations similar to the water-soluble DOC we measured in our filter extracts in Fairbanks during January and February of 2022 (Figure 4). During the summer, $PM_{2.5}$ and OA concentrations are highly variable due to the influence of wildfire smoke: the summer of 2021 (depicted in Figure 9b) was only moderately impacted by wildfire smoke, while summers with severe wildfire smoke have much larger OA and BrC concentrations. Once the monthly average OA concentration was determined, we used the average MAC_λ from water-soluble organic carbon measured with the House site samples to calculate $j_{BrC \rightarrow 3C*}$. We do not determine the fraction of OA that is light-absorbing BrC, but instead we determine the light absorbance by the BrC within the entire OA population using the OA-averaged MAC values.

320   **Table S1.** Sample collection dates and times for 2022 ALPACA campaign

Composite Name [a]	House Site:		CTC Site:	
	Filter Sample Collection		*Filter Sample Collection*	
	Start	End	Start	End
1/15	1/13 17:10	1/17 09:41	N/A	N/A
1/21 [b]	1/17 10:00	1/25 09:30	1/17 13:59	1/25 08:52
1/27	1/26 10:00	1/28 09:30	1/26 10:20	1/28 09:06
1/31 [c]	1/29 10:00	2/3 09:30	1/29 09:31	2/3 09:00
2/4	2/3 10:00	2/6 09:30	2/3 09:46	2/6 09:04
2/7	2/6 10:00	2/8 09:30	2/6 09:38	2/8 08:59
2/14	2/8 10:00	2/21 09:30	2/8 09:30	2/21 09:05
2/22	2/21 10:00	2/23 09:30	2/21 09:33	2/23 09:05
2/24	2/23 10:00	2/26 09:30	2/23 09:45	2/26 08:41
Field Blank [d]	*House Field Blank Composite*		*CTC Field Blank Composite*	
	1/18 09:00 (30 second collection)		2/9 09:34	2/9 09:37
	1/25 09:00 (30 second collection)		2/20 09:29	2/20 09:31

[a] Composites are named by the midpoint date of the sampling period. Start and end times are in 24-hr format.
[b] The House site contains a 43.5-hour filter sample between 1/17 13:59 and 1/19 9:30 which was included in the 1/21 composite. When this filter was extracted into water, it had higher solute concentrations purely based on having a longer
325   filter collection time compared to the 24-hour samples. The data reported for the 1/21 sample is corrected for the high solute concentrations due to the longer sampling time.
[c] Between 1/30 and 2/3, we collected separate day and night filter samples at the CTC site, covering 7 and 17 hours, respectively.
[d] Field blanks were prepared for each site by compositing the corresponding two field blank filter samples.
330

Table S2. pH values of particle extracts.

Site	Sample		pH	
			Extraction Solution [a]	PM Extract [b]
House	1/15		1.3	0.87
	1/21		1.3	1.23
	1/27		5.6	4.39 [c]
	1/31		1.3	1.28
	2/4		1.3	1.10
	2/7		1.3	0.88
	2/14		1.3	1.22
	2/22		1.3	1.10
	2/24		1.3	1.15
	Field Blank		1.3	1.31
CTC	1/21		1.3	1.26
	2/7		1.3	1.22
	1/21		5.0	5.11
	2/22		5.0	5.04 [d]
	2/24		5.0	4.82 [e]
	2/14 [f]	10.0	1.3	1.01
		2.0	1.3	1.02
		0.70	1.3	1.01
		0.40	1.7 [g]	1.08
		0.30	1.8 [g]	1.13
	Field Blank		5.0	4.90 [h]

[a] This is the pH of the H_2SO_4 solution (generally either 5×10^{-2} or 1×10^{-5} M) that was used to extract the $PM_{2.5}$ filters.

[b] This is the pH of the particle extract, which was used for photochemical experiments.

[c] The pH after extraction was 6.73, which was adjusted to 4.39 with 75 µL of 10 mM H_2SO_4.

[d] The pH after extraction was 5.82, which was adjusted to 5.04 with 53 µL of 10 mM H_2SO_4.

[e] The pH after extraction was 5.39, which was adjusted to 4.82 with 20 µL of 10 mM H_2SO_4 and 13 µL of 10 mM NaOH.

[f] A series of dilutions were made for this sample, where different volumes of H_2SO_4 solution were used to extract each filter square. The numbers on the different rows for this sample (10.0, 2.0, 0.70, etc.) represent the volume of solution (in mL) used for a given dilution. The solution volume used for the other samples was 1.0 mL.

[g] After using rotary evaporation to remove water, the pH of the 0.4x and 0.3x solutions are both expected to be 1.3.

[h] The pH after extraction was 6.81, which was adjusted to 4.90 with 85 µL of 10 mM H_2SO_4.

345 **Table S3.** Chemical probes (P) and their rate constants with oxidants (k_{P+Ox})

Probe		$k_{P+•OH}$ (M^{-1} s^{-1})	k_{P+1O2*} (M^{-1} s^{-1})	k_{P+3C*} (M^{-1} s^{-1})
Benzoic Acid [a]	pH 1	4.30×10^9	-	-
	pH 5	5.69×10^9		
Furfuryl Alcohol		1.50×10^{10} [b]	8.06×10^7 [c]	-
Syringol (SYR) [d]	pH 1	$1.5(\pm0.7)\times10^{10}$	$3.6(\pm0.7)\times10^7$	$6.7(\pm1.5)\times10^9$ [e]
	pH 5	$2.0(\pm0.4)\times10^{10}$		

[a] At pH 1, where there is no significant dissociation of benzoic acid into benzoate, the rate constant is equal to the value for benzoic acid (4.3×10^9 M^{-1} s^{-1}; Anastasio and McGregor, 2001; Ashton et al., 1995; Wander et al., 1968). At pH 5 where only 13.4% of benzoic acid/benzoate is protonated, the rate constant is a mole-fraction-weighted rate constant for the
350 reaction of •OH with benzoate (5.9×10^9 M^{-1} s^{-1}; Anastasio and McGregor, 2001) and benzoic acid. The resulting a mole-fraction-weighted rate constant is 5.69×10^9 M^{-1} s^{-1}.

[b] The rate constant of FFA with •OH was reported by (Ross and Ross, 1977).

[c] Furfuryl alcohol rate constant is temperature-corrected to 10 °C (Appiani et al., 2017). Other rate constants listed in the table are not adjusted for temperature.

355 [d] $k_{SYR+•OH}$ and $k_{SYR+3C*}$ were measured at pH 2. We use the pH 2 •OH values for our pH 1 solutions and use the pH 2 rate constants for both pH 1 and pH 5 experiments (Ma et al., 2022; Smith et al., 2015).

[e] Smith et al. (2015) measured $k_{SYR+3C*}$ using triplet 3,4-dimethoxybenzaldehyde (^{3}DMB*) at pH 2 and 5 and found notable differences in k_{P+3C*}: $6.7(\pm1.5)\times10^9$ at pH 2 and $3.5(\pm0.8)\times10^9$ M^{-1} s^{-1} at pH 5. The pH dependence is because the pKa of 3,4-DMB is 3.3, suggesting the pH dependence is specific to the triplet state of 3,4-DMB and therefore should not be
360 applied to the entire pool of ^{3}C* measured by syringol. We assume the k_{P+3C*} at both pH 1 and pH 5 is equivalent to $6.7(\pm1.5)\times10^9$ M^{-1} s^{-1}, the rate constant measured by Smith et al. (2015) at pH 2.

Table S4. Parameters for calculating mass transport of $^\bullet OH(g)$ to particles and drops: Part I

Water Content [a]	Aerosol Liquid Water Conditions	Cloud/Fog Drop Conditions
PM-mass/H$_2$O-mass ratio (µg-PM/µg-H$_2$O)	1	6×10^{-5}
Particle/Drop Diameter (µm)	0.7	14
Particle/Drop Volume (cm^3)	1.8×10^{-13}	1.4×10^{-9}
assume $C_s = 0$ [b]		
Mass Accommodation Coefficient	1	
$^\bullet OH(g)$ (mlc cm^{-3})	3.0×10^5	

[a] The water content of particles qualitatively names the condition quantitatively defined by the PM-mass/H$_2$O-mass ratio, i.e., the mass of a dry particle relative to the mass of liquid water.

[b] Assuming the concentration of $^\bullet OH$ at the surface of the particle (C_s) is 0 makes our calculated $P_{\bullet OH,MT}$ an upper-bound estimate.

Table S5. Parameters for calculating mass transport of •OH(g) to particles and drops: Part II [a]

Sample	Gas-Phase Diffusion Coefficient (cm^2 s^{-1})	Mean Molecular Speed (cm s^{-1})	Mean Free Path (cm) (assumes zero kinetic order theory)
1/15	0.20	5.62×10^4	1.1×10^{-5}
1/21	0.19	5.59×10^4	1.0×10^{-5}
1/27	0.19	5.60×10^4	1.0×10^{-5}
1/31	0.18	5.49×10^4	9.9×10^{-5}
2/4	0.20	5.64×10^4	1.1×10^{-5}
2/7	0.20	5.61×10^4	1.0×10^{-5}
2/14	0.20	5.62×10^4	1.1×10^{-5}
2/22	0.21	5.76×10^4	1.1×10^{-5}
2/24	0.22	5.78×10^4	1.1×10^{-5}

[a] Equations are from Seinfeld & Pandis (2016).

375 **Table S6.** Parameters for calculating mass transport of $^{\bullet}OH(g)$ to particles and drops: Part III [a]

Sample	Aerosol Liquid Water Conditions [b]					Cloud/Fog Drop Conditions [b]				
	Knudsen Number (Kn)	Fuch's Transition Regime Correction Factor	Continuum Flux (mlc drop^{-1} s^{-1})	Transition Flux (mlc drop^{-1} s^{-1})	$P_{\bullet OH,MT}$ (M s^{-1})	Knudsen Number (Kn)	Fuch's Transition Regime Correction Factor	Continuum Flux (mlc drop^{-1} s^{-1})	Transition Flux (mlc drop^{-1} s^{-1})	$P_{\bullet OH,MT}$ (M s^{-1})
1/15	0.30	0.80	26	21	1.9×10^{-7}	1.50×10^{-2}	0.989	520	514	5.9×10^{-10}
1/21	0.30	0.80	25	20	1.9×10^{-7}	1.48×10^{-2}	0.989	510	504	5.8×10^{-10}
1/27	0.30	0.80	26	20	1.9×10^{-7}	1.49×10^{-2}	0.989	513	508	5.9×10^{-10}
1/31	0.28	0.81	24	19	1.8×10^{-7}	1.42×10^{-2}	0.990	479	474	5.5×10^{-10}
2/4	0.30	0.79	26	21	1.9×10^{-7}	1.52×10^{-2}	0.989	527	521	6.0×10^{-10}
2/7	0.30	0.80	26	21	1.9×10^{-7}	1.50×10^{-2}	0.989	517	511	5.9×10^{-10}
2/14	0.30	0.80	26	21	1.9×10^{-7}	1.50×10^{-2}	0.989	520	514	5.9×10^{-10}
2/22	0.32	0.78	28	22	2.1×10^{-7}	1.60×10^{-2}	0.989	567	560	6.5×10^{-10}
2/24	0.32	0.78	29	22	2.1×10^{-7}	1.61×10^{-2}	0.989	574	567	6.6×10^{-10}

[a] Equations are from Seinfeld & Pandis (2016). $P_{\bullet OH,MT}$ is the rate of $^{\bullet}OH(g)$ partitioning to the particles/drops, expressed in terms of the aqueous volume, i.e., mol-$^{\bullet}OH$ L^{-1}-solution s^{-1}.

[b] The water content of particles qualitatively names the condition quantitatively defined by the PM-mass/H$_2$O-mass ratio,
380 i.e., the mass of dry particle solutes relative to the mass of liquid water. Cloud/fog droplets have a higher liquid water content and larger particle diameters than aerosol particles (Table S4). Particle diameter is especially important for mass transport because $P_{\bullet OH,MT}$ (expressed in terms of liquid volume) decreases with increasing particle diameter, meaning aerosol liquid water has much higher $P_{\bullet OH,MT}$ compared to cloud/fog drop conditions.

385 **Table S7.** Characterization of sample composite periods: average PM$_{2.5}$, temperature, relative humidity, and actinic flux

Composite	PM$_{2.5}$ [a] (μg m^{-3})	Average Temp.[b] (°C)	Relative Humidity [c] (%)	Albedo (fraction) [d]	Downwelling $I_{\lambda,310\text{-}550\text{ nm}}$ [e] (photon cm^{-2} s^{-1})	
					Solar Noon	Midday Three-Hour Average
1/15	7.5	-19	N/A	N/A	N/A	N/A
1/21	12.0	-22	86	0.82	1.0×10^{16}	7.2×10^{15}
1/27	17.7	-21	77	0.81	1.7×10^{16}	1.2×10^{16}
1/31	26.1	-31	75	0.72	3.2×10^{16}	2.3×10^{16}
2/4	8.6	-18	80	0.85	1.0×10^{16}	8.7×10^{15}
2/7	4.3	-20	77	0.90	1.3×10^{16}	1.1×10^{16}
2/14	7.2	-20	80	0.87	2.7×10^{16}	2.0×10^{16}
2/22	3.6	-7	90	0.96	1.4×10^{16}	1.1×10^{16}
2/24	12.5	-5	90	0.85	3.5×10^{16}	2.9×10^{16}

[a] PM$_{2.5}$ measured at the NCore site by the Alaska Department of Environmental conservation. Data is available at https://www.epa.gov/outdoor-air-quality-data/download-daily-data.

[b] Temperature measured at the CTC site. Data is available at https://arcticdata.io/catalog/portals/ALPACA/Data.

390 [c] Relative Humidity reported at Airport Road by Environmental Research Division's Data Access Program (ERDDAP). Data is available at https://erddap.sensors.ioos.us/erddap/tabledap/alaska-dot-rwis-255.html.

[d] Surface albedo determined using the ratio of the upwelling j_{NO2} to the downwelling j_{NO2} determined at the NCore site.

[e] Downwelling actinic fluxes measured using the Diode-Array Actinic Flux Spectroradiometer at the NCore site in downtown Fairbanks (Simpson et al., 2024). The "Solar Noon" column reflects daily I_λ measured at 13:30, around solar

395 noon, averaged over a given composite. The "Downwelling Midday Three-Hour Average" column reflects the daily I_λ averaged between 12:00 and 15:00 – the peak three hours of sunlight, then again averaged over each day in each composite. We converted the downwelling actinic flux to the total (downwelling and upwelling) flux by multiplying it by the sum of (1 + albedo).

 Table S8. Parameters used in TUV to model actinic fluxes during ALPACA

Latitude		64.840
Longitude		-147.720
Overhead Column Ozone (du) [a]		300
Surface Albedo (fraction)		0.85
Ground Elevation (km above sea level)		0.15
Measurement Altitude (km above sea level)		0.16
Clouds [a]	Optical Depth	0
	Base	4
	Top	5
Aerosols [a]	Optical Depth	0.235
	S-S Albedo	0.99
	Alpha	1

[a] Standard input parameters in the TUV model; these are not specific to Fairbanks.

Table S9. Characterization of water-soluble brown carbon in PM extracts (PME)

Site	Sample		PM-Mass/H$_2$O-Mass Ratio (µg µg^{-1}) [a]	[DOC]$_{PME}$ (mM)	MAC$_{300}$ (m^2 g-C^{-1}) [b]	MAC$_{365}$ (m^2 g-C^{-1}) [b]	AAE [c]	E2/E3 [d]
House	1/15, pH 1		2.8($\pm$0.2)$\times10^{-4}$	2.8($\pm$0.2)	3.75	1.01	9.4	6.4
	1/21, pH 1		2.6($\pm$0.1)$\times10^{-4}$	3.0($\pm$0.2)	3.31	0.863	9.1	6.5
	1/27, pH 4.5		3.0($\pm$0.6)$\times10^{-4}$	3.18($\pm$0.06)	3.78	1.05	8.2	6.4
	1/31, pH 1		3.2($\pm$0.1)$\times10^{-4}$	4.90($\pm$0.06)	4.04	0.964	8.8	7.1
	2/4, pH 1		1.7($\pm$0.3)$\times10^{-4}$	1.7($\pm$0.2)	4.61	1.07	9.3	7.4
	2/7, pH 1		4.7($\pm$0.1)$\times10^{-4}$	1.84($\pm$0.02)	2.66	0.583	10.2	8.0
	2/14, pH 1		1.9($\pm$0.6)$\times10^{-4}$	2.22($\pm$0.04)	3.20	0.768	9.4	7.3
	2/22, pH 1		1.8($\pm$0.2)$\times10^{-4}$	2.24($\pm$0.09)	1.88	0.402	10.2	7.9
	2/24, pH 1		3.3($\pm$0.4)$\times10^{-4}$	3.0($\pm$0.1)	2.65	0.680	9.4	6.8
	Field Blank, pH 1		1.2($\pm$0.2)$\times10^{-4}$	0.23($\pm$0.01)	0.246	0	N/A	
CTC	1/21, pH 1		2.1($\pm$0.1)$\times10^{-4}$	2.70($\pm$0.06)	3.41	0.999	8.3	6.4
	1/21, pH 5		2.1($\pm$0.1)$\times10^{-4}$	2.70($\pm$0.02)	2.16	0.577	9.1	7.0
	2/7, pH 1		1.8($\pm$0.1)$\times10^{-4}$	1.86($\pm$0.03)	3.55	1.10	7.3	5.8
	2/22, pH 5		2.2($\pm$0.4)$\times10^{-4}$	2.15($\pm$0.03)	2.12	0.611	7.7	6.7
	2/24, pH 5		2.1($\pm$0.1)$\times10^{-4}$	2.99($\pm$0.06)	2.44	0.757	7.2	6.2
	2/14, pH 1 [e]	10	1.79($\pm$0.04)$\times10^{-5}$	0.227($\pm$0.003)	3.21	0.837	8.7	7.3
		2.0	8.9($\pm$0.2)$\times10^{-5}$	1.15($\pm$0.01)	3.13	0.831	8.9	7.1
		0.70	2.55($\pm$0.04)$\times10^{-4}$	2.96($\pm$0.01)	3.65	1.00	8.9	6.7
		0.40	4.46($\pm$0.09)$\times10^{-4}$	5.14($\pm$0.06)	3.20	0.926	8.6	6.3
		0.30	6.0($\pm$0.1)$\times10^{-4}$	6.55($\pm$0.04)	3.18	0.966	7.9	6.0
	Field Blank, pH 5		1.7($\pm$0.3)$\times10^{-4}$	0.122($\pm$0.002)	0.878	0.328	N/A	

[a] PM-mass/H$_2$O-mass ratio reflects the concentration of a given extract, expressed as the ratio of dry PM mass extracted from a filter to the amount of liquid water in the extract. The extracted PM mass was measured from filters extracted into Milli-Q water, and therefore we list the same PM Mass/H$_2$O Mass ratio for the two extracts of the CTC 1/21 composite prepared separately at pH 1.3 and pH 5. The blank filters have non-zero PM-mass/H$_2$O-mass ratios because part of the filter degrades upon extraction.

[b] MAC$_\lambda$ values are calculated using the absorbance and DOC concentrations measured in the PM extracts. MAC$_\lambda$ values reported above use the DOC concentrations measured in the extracts, blank corrected for field blank DOC (reported for the two sites above). This assumes that the minor DOC contamination has minimal impact on the measured absorbance of extracts, a fair assumption because the background DOC concentrations are low (< 10% of the measured DOC concentration) and the MAC$_\lambda$ of the blanks are lower than the field samples.

[c] AAE is the absorption Angstrom exponent, calculated between 300 and 450 nm.

[d] E2/E3 is the ratio of BrC absorbance at 250 nm to that at 365 nm (Helms et al., 2008; Peuravuori and Pihlaja, 1997).

[e] For the CTC 2/14 dilution series, the PM-mass/H$_2$O-mass ratio was only determined for the 0.70 dilution sample, the PM-mass/H$_2$O-mass ratio values for the 10, 2.0, 0.40, and 0.30 dilutions were calculated by extrapolation. See Table S2 for a description of this dilution series. The DOC concentrations and absorbance parameters were measured for each dilution.

405

410

415

420

Table S10. Solar simulator experimental data I: p-HBA formation and first-order rate constants for probe loss

Site	Sample		Rate of p-HBA Production (μM min^{-1}) [b]	Experimental Probe Loss (j_{2NB} = 0.0045 s^{-1}) [a]		
				$k'_{EXP,BA}$ (s^{-1}) [b]	$k'_{EXP,FFA}$ (s^{-1})	$k'_{EXP,SYR}$ (s^{-1})
House	1/15, pH 1		2.2($\pm$0.2)$\times10^{-3}$	8.8($\pm$0.7)$\times10^{-6}$	1.2($\pm$0.2)$\times10^{-4}$	9.2($\pm$1.1)$\times10^{-4}$
	1/21, pH 1		1.0($\pm$0.1)$\times10^{-3}$	7.9($\pm$0.7)$\times10^{-6}$	1.3($\pm$0.05)$\times10^{-4}$	1.2($\pm$0.05)$\times10^{-3}$
	1/27, pH 4.5		6.1($\pm$0.1)$\times10^{-3}$	2.7($\pm$0.2)$\times10^{-6}$	1.2($\pm$0.05)$\times10^{-4}$	1.5($\pm$0.07)$\times10^{-4}$
	1/31, pH 1		3.2($\pm$0.1)$\times10^{-3}$	7.7($\pm$0.5)$\times10^{-6}$	1.4($\pm$0.07)$\times10^{-4}$	9.2($\pm$0.5)$\times10^{-4}$
	2/4, pH 1		1.2($\pm$0.2)$\times10^{-3}$	6.5($\pm$1.1)$\times10^{-6}$	1.4($\pm$0.9)$\times10^{-3}$	3.8($\pm$0.2)$\times10^{-4}$
	2/7, pH 1		6.3($\pm$0.9)$\times10^{-4}$	3.3($\pm$0.2)$\times10^{-6}$	8.6($\pm$0.2)$\times10^{-5}$	7.9($\pm$0.7)$\times10^{-4}$
	2/14, pH 1		3.2($\pm$0.2)$\times10^{-3}$	1.8($\pm$0.09)$\times10^{-5}$	1.1($\pm$0.09)$\times10^{-4}$	9.2($\pm$0.5)$\times10^{-4}$
	2/22, pH 1		1.1($\pm$0.1)$\times10^{-3}$	5.0($\pm$0.5)$\times10^{-6}$	8.3($\pm$0.5)$\times10^{-5}$	7.7($\pm$0.5)$\times10^{-4}$
	2/24, pH 1		7.4($\pm$1.1)$\times10^{-4}$	7.0($\pm$0.5)$\times10^{-6}$	1.2($\pm$0.07)$\times10^{-4}$	7.4($\pm$0.5)$\times10^{-4}$
	Field Blank, pH 1		1.2($\pm$0.2)$\times10^{-4}$	1.6($\pm$0.09)$\times10^{-6}$	1.1($\pm$0.05)$\times10^{-5}$	9.2($\pm$1.4)$\times10^{-6}$
CTC	1/21, pH 1		8.3($\pm$1.6)$\times10^{-4}$	7.9($\pm$0.2)$\times10^{-6}$	2.6($\pm$0.2)$\times10^{-5}$	1.4($\pm$0.07)$\times10^{-3}$
	1/21, pH 5		3.2($\pm$0.2)$\times10^{-4}$	3.4($\pm$0.09)$\times10^{-6}$	1.4($\pm$0.07)$\times10^{-4}$	5.0($\pm$0.2)$\times10^{-4}$
	2/7, pH 1		5.9($\pm$0.2)$\times10^{-4}$	5.4($\pm$0.2)$\times10^{-6}$	1.3($\pm$0.09)$\times10^{-4}$	9.7($\pm$0.5)$\times10^{-4}$
	2/22, pH 5		1.8($\pm$0.2)$\times10^{-4}$	1.5($\pm$0.2)$\times10^{-6}$	8.1($\pm$0.2)$\times10^{-5}$	7.2($\pm$0.9)$\times10^{-5}$
	2/24, pH 5		2.0($\pm$0.4)$\times10^{-4}$	1.5($\pm$0.1)$\times10^{-6}$	9.5($\pm$0.9)$\times10^{-5}$	1.5($\pm$0.09)$\times10^{-4}$
	2/14, pH 1 [c]	10	2.1($\pm$0.4)$\times10^{-4}$	2.4($\pm$0.1)$\times10^{-6}$	2.9($\pm$0.1)$\times10^{-5}$	1.1($\pm$0.07)$\times10^{-4}$
		2.0	6.3($\pm$0.7)$\times10^{-4}$	4.7($\pm$0.2)$\times10^{-6}$	1.0($\pm$0.07)$\times10^{-4}$	3.1($\pm$0.2)$\times10^{-4}$
		0.70	4.5($\pm$1.4)$\times10^{-4}$	7.7($\pm$0.5)$\times10^{-6}$	2.5($\pm$0.1)$\times10^{-4}$	5.4($\pm$0.5)$\times10^{-4}$
		0.40	5.2($\pm$0.9)$\times10^{-4}$	5.6($\pm$0.7)$\times10^{-6}$	2.7($\pm$0.2)$\times10^{-4}$	5.0($\pm$0.2)$\times10^{-4}$
		0.30	7.2($\pm$0.5)$\times10^{-4}$	4.7($\pm$0.5)$\times10^{-6}$	2.0($\pm$0.1)$\times10^{-4}$	4.3($\pm$0.2)$\times10^{-4}$
	Field Blank, pH 5		4.5($\pm$0.9)$\times10^{-5}$	2.7($\pm$1.6)$\times10^{-7}$	1.4($\pm$0.5)$\times10^{-6}$	0.9($\pm$1.8)$\times10^{-6}$

[a] The k' for experimental probe loss is the pseudo-first order rate constant for probe loss observed from every experiment where 1 mL of PME was spiked with 10 μM of each probe and illuminated in our solar simulator. These values are normalized to a single j_{2NB} value to account for variations in the intensity of the lamp in the solar simulator between experiment days.

[b] The rate of p-HBA production and the loss of BA were both used to calculate [$^\bullet$OH]. The [$^\bullet$OH] reported here is the average of the [$^\bullet$OH] determined by both methods.

[c] See Table S2 for a description of this dilution series.

425

430

Table S11. Solar simulator experimental data II: Rate of light absorbance, screening factor, and inhibition factor

Site	Sample		$R_{abs,EXP,PME}$ (mol L^{-1} s^{-1}) [a]	Screening Factor (300 - 500 nm, unitless) [b]	Inhibition Factor (*IF*, unitless)		
					FFA [c]	SYR (uncorrected)	SYR$_{corr}$ (corrected) [d]
House	1/15, pH 1		8.0×10^{-6}	0.93	0.57(±0.093)	0.21(±0.075)	0.38(±0.15)
	1/21, pH 1		7.9×10^{-6}	0.94	0.78(±0.065)	0.84(±0.11)	1
	1/27, pH 4.5		1.1×10^{-5}	0.93	0.35(±0.034)	0.063(±0.0080)	0.18(±0.028)
	1/31, pH 1		1.6×10^{-5}	0.89	1.5(±0.14)	0.20(±0.040)	
	2/4, pH 1		5.3×10^{-6}	0.96	0.36(±0.034)	0.23(±0.039)	0.64(±0.13)
	2/7, pH 1		2.9×10^{-6}	0.97	0.99(±0.11)	0.93(±0.21)	0.94(±0.23)
	2/14, pH 1		4.9×10^{-6}	0.96	0.59(±0.057)	1.1(±0.13)	1
	2/22, pH 1		2.5×10^{-6}	0.97	0.98(±0.55)	1.3(±0.12)	1
	2/24, pH 1		4.7×10^{-6}	0.95	0.68(±0.046)	0.64(±0.080)	0.94(±0.13)
	Field Blank, pH 1		1.0×10^{-7}	1.00	0.70(±0.060)	0.95(±0.058)	1
CTC	1/21, pH 1		9.0×10^{-6}	0.86	0.67(±0.055)	0.99(±0.17)	1
	1/21, pH 5		1.1×10^{-5}	0.87	0.53(±0.070)	0.14(±0.047)	0.26(±0.090)
	2/7, pH 1		1.1×10^{-6}	0.84	0.59(±0.050)	1.1(±0.10)	1
	2/22, pH 5		4.9×10^{-6}	0.87	0.76(±0.045)	0.018(±0.0050)	0.024(±0.0070)
	2/24, pH 5		9.5×10^{-6}	0.88	0.63(±0.065)	0.033(±0.016)	0.053(±0.026)
	2/14, pH 1 [f]	10	6.4×10^{-7}	1.00	0.78(±0.049)	0.54(±0.050)	0.69(±0.078)
		2.0	3.2×10^{-6}	0.98	0.59(±0.044)	0.29(±0.037)	0.49(±0.072)
		0.70	9.8×10^{-6}	0.93	0.35(±0.024)	0.064(±0.030)	0.18(±0.088)
		0.40	1.6×10^{-5}	0.89	nd [e]		0.090
		0.30	2.5×10^{-5}	0.88	1.2(±0.10)	0.066(±0.026)	
	Field Blank, pH 5		2.7×10^{-7}	1.00	0.95(±0.30)	1.2(±0.14)	1

[a] $R_{abs,EXP,PME}$ is the rate of light absorbance in the PM extract in the solar simulator, summed between 300 and 550 nm. Values were calculated for a photon flux condition of $j_{2NB} = 0.0045$ s^{-1}, the calculated rate constant for 2NB photolysis on midday of February 1st in Fairbanks under clear sky conditions.

[b] Screening factor calculation explained in Section S2.

[c] When IF_{FFA} is greater than 1, we assume there is no suppression of [^{3}C*] due to quenching by DOC and therefore IF_{FFA} is equal to 1, meaning $IF_{SYR,corr}$ is equal to IF_{SYR} (Ma et al., 2023).

[d] When IF_{SYR} is greater than IF_{FFA}, we assume no inhibition of SYR occurs and set $IF_{SYR,corr}$ equal to 1 (Ma et al., 2023).

[e] Due to limited available sample volume, *IF* values were not measured for the CTC 2/14 0.40 dilution series sample. Instead, this *IF* value was estimated for this sample using the linear relationship between $1/IF_{SYR,corr}$ and [DOC]$_{PME}$ from the other filutions (Ma et al., 2023).

[f] See Table S2 for a description of this dilution series.

445 **Table S12.** Exploring sources of $^\bullet$OH in PM extracts

Site	Sample	$P_{\bullet OH,EXP,PME}$ (M s^{-1}) [a]	NO_2^- (µM)	NO_3^- (µM)	$P_{\bullet OH,NO2-}$ (M s^{-1}) [a,b]	$P_{\bullet OH,NO3-}$ (M s^{-1}) [a,b]	P_{HOOH} (M s^{-1}) [a]
House	1/15, pH 1	3.8×10^{-9}	0	272	0	2.4×10^{-11}	6.9×10^{-9}
	1/21, pH 1	2.5×10^{-9}	0	268	0	2.4×10^{-11}	8.3×10^{-9}
	1/27, pH 4.5	1.0×10^{-9}	0	437	0	3.9×10^{-11}	3.6×10^{-9}
	1/31, pH 1	9.3×10^{-9}	0	291	0	2.6×10^{-11}	2.2×10^{-8}
	2/4, pH 1	1.4×10^{-9}	0	170	0	1.5×10^{-11}	4.9×10^{-9}
	2/7, pH 1	7.7×10^{-10}	0	84	0	7.6×10^{-12}	4.1×10^{-9}
	2/14, pH 1	1.6×10^{-9}	0	163	0	1.5×10^{-11}	5.7×10^{-9}
	2/22, pH 1	1.7×10^{-9}	0	145	0	1.3×10^{-11}	2.5×10^{-9}
	2/24, pH 1	2.0×10^{-9}	1	276	1.7×10^{-11}	2.5×10^{-11}	4.8×10^{-9}

[a] All rates shown here are normalized to $j_{2NB,AK} = 0.0045$ s^{-1} conditions. $P_{\bullet OH,EXP,PME}$ is the estimated rate of $^\bullet$OH formation in the extract, calculated from the measured [$^\bullet$OH] (equation S6). $P_{\bullet OH,NO2-}$ and $P_{\bullet OH,NO3-}$ are the rates of $^\bullet$OH formation from the direct photolysis of nitrite and nitrate, respectively, in the extract and P_{HOOH} is the production rate of HOOH
450 determined in each extract (Sunday et al., 2024).

[b] $j_{NO3-\rightarrow\bullet OH}$ (1.4×10^{-7} s^{-1}) and $j_{NO2-\rightarrow\bullet OH}$ (2.6×10^{-5} s^{-1}) are rate constants reported by Anastasio & McGregor (2001) for our solar simulator, normalized to Davis midday winter solstice sunlight, where $j_{2NB} = 0.007$ s^{-1}. Here, we adjusted the rate constants for $^\bullet$OH formation from nitrate and nitrite to Fairbanks conditions on February 1st ($j_{2NB,AK} = 0.0045$ s^{-1}), i.e., $j_{NO3-\rightarrow\bullet OH} = 9.0\times10^{-8}$ s^{-1} and $j_{NO2-\rightarrow\bullet OH} = 1.7\times10^{-5}$ s^{-1}.

455

Table S13. Kinetic model for dilution series: Dominant loss pathways for oxidants [a]

Sample: CTC 2/14, pH 1	k' for •OH loss to DOC (s^{-1}) [b]	Percent of ^{3}C* loss [c]		Percent of ^{1}O$_2$* loss	
		to DOC	to O$_2$	to DOC	to H$_2$O
PME 10	7.9×10^4	2	98	0.01	99.99
PME 2.0	4.1×10^5	9	91	0.04	99.96
PME 0.70	1.1×10^6	20	80	0.10	99.90
PME 0.40	1.8×10^6	31	69	0.17	99.83
PME 0.30	2.3×10^6	36	64	0.22	99.78
Extrapolation to ALW	8.6×10^9	99.95	0.05	89	11

[a] Dilution series was performed on the CTC 2/14 pH 1 composite. See Table S2 for more information about the dilution series.

[b] First-order rate constant for OH loss due to reaction with DOC, estimated as the product of the measured DOC concentration and the second-order rate constant for DOC + •OH, $3.8(\pm1.9) \times 10^8$ L mol-C^{-1} s^{-1}, from Arakaki et al. (2013).

[c] Rate constants for triplets reacting with DOC and dissolved oxygen are in Section S4. [O$_2$] in Fairbanks particle water was determined using the temperature-adjusted Henry's Law constant (Sander, 2023) assuming solutions are air saturated. In laboratory conditions at 10 °C, [O$_2$] was assumed to be 272 µM; this value was used for the dilution series calculations shown in the table. For ALW conditions predicted in Fairbanks and shown in the table, we used the average temperature for this sample (-20 °C; Table S7).

470 **Table S14.** Parameters for modelling photooxidant concentrations from PM extracts to aerosol liquid water conditions

Oxidant	Rate Constant	Value	Source
$^\bullet$OH	$k_{\bullet OH+DOC}$ (L mol^{-1}-C s^{-1})	$3.8(\pm1.9)\times10^8$	(Arakaki et al., 2013)
$^1O_2*$	$k'_{1O2*+H2O}$ (s^{-1})	$2.8(\pm0.02)\times10^5$	(Appiani et al., 2017)
	$k_{1O2*+DOC}$ (L mol^{-1}-C s^{-1})	1.0×10^5	(Ma et al., 2023)
$^3C*$	$k_{3C*+DOC,SYR}$ (L mol^{-1}-C s^{-1}) [a]	7.0×10^7	(Ma et al., 2024)
	$k_{3C*+DOC,FFA}$ (L mol^{-1}-C s^{-1}) [b]	1.0×10^7	(Ma et al., 2024)
	k_{3C*+O2} (M^{-1} s^{-1})	2.8×10^9	(Kaur et al., 2019)

[a] This rate constant for reactions of DOC with oxidizing $^3C*$ was measured by Ma et al. (2024) using syringol as a probe.
[b] This rate constant for the reaction of DOC with the entire pool of $^3C*$ was measured by Ma et al. (2024) using furfuryl
475   alcohol as a probe for $^1O_2*$. Singlet oxygen is a proxy for the entire pool of $^3C*$ since every triplet should be able to
produce $^1O_2*$, while only oxidizing triplets can react with syringol.

Table S15. Estimated aerosol liquid water characteristics: Rate of light absorbance, DOC, and concentration factor

Site	Sample	$R_{abs,AK,ALW}$ (mol L^{-1} s^{-1}) [a]	[DOC]$_{ALW}$ (M)	CF, or [DOC]$_{ALW}$ / [DOC]$_{PME}$ [b]
House	1/15, pH 1	3.0×10^{-2}	16($\pm$1)	6.2×10^{3}
	1/21, pH 1	2.0×10^{-2}	17($\pm$1)	6.0×10^{3}
	1/27, pH 4.5	4.3×10^{-2}	19.0($\pm$0.4)	6.4×10^{3}
	1/31, pH 1	6.5×10^{-2}	21.1($\pm$0.3)	4.5×10^{3}
	2/4, pH 1	4.9×10^{-2}	22($\pm$2)	1.5×10^{4}
	2/7, pH 1	9.9×10^{-2}	62($\pm$1)	3.9×10^{4}
	2/14, pH 1	7.3×10^{-2}	23.6($\pm$0.5)	1.2×10^{4}
	2/22, pH 1	1.6×10^{-2}	15.2($\pm$0.7)	7.6×10^{3}
	2/24, pH 1	2.4×10^{-2}	6.2($\pm$0.2)	2.3×10^{3}
CTC	1/21, pH 1	1.7×10^{-2}	9.6($\pm$0.3)	3.7×10^{3}
	1/21, pH 5	1.9×10^{-2}	9.6($\pm$0.2)	3.7×10^{3}
	2/14, pH 1	8.7×10^{-2}	23.0($\pm$0.1)	8.3×10^{3}
	2/7, pH 1	3.4×10^{-3}	47($\pm$1)	2.7×10^{4}
	2/22, pH 5	1.8×10^{-2}	8.9($\pm$0.2)	5.4×10^{3}
	2/24, pH 5	5.5×10^{-2}	4.8($\pm$0.1)	1.7×10^{3}

480

[a] Rate of light absorbance in particle water under the midday Fairbanks sunlight measured for the middle day of each composite, $R_{abs,AK,ALW}$, calculated over the range of 300 to 550 nm.

[b] The ratio of DOC concentration in aerosol liquid water compared to that in the lab PM extract. This is the factor by which the PME concentration of a stable species (i.e., not a photooxidant) is multiplied by to estimate the ALW concentration.

485 The ratio was determined as described in Section S6. For the dilution series sample (CTC 2/14), the CF is expressed based on the DOC concentration expected for a filter square extracted with the standard volume (1.0 mL) of solution, which was interpolated from the DOC values of the dilutions.

Table S16. Modelling photooxidant production in PME and ALW under Fairbanks actinic flux conditions

	Sample	$[O_2]_{ALW}$ (µM) [a]	$P_{\bullet OH,MT}$ (M s^{-1}) [b] PME (×10^{10})	ALW (×10^7)	k'_{DOC} [c] (s^{-1}) PME (×10^{-5})	ALW (×10^{-9})	Loss of $^3C^*$ to DOC (%) PME	ALW	Loss of $^3C^*$ to O$_2$ (%) PME	ALW	$\Delta P_{1O2*}/\Delta DOC$ (10^5 s^{-1})	Loss of $^1O_2^*$ to DOC (%) PME	ALW	Loss of $^1O_2^*$ to H$_2$O (%) PME	ALW
House	1/15, pH 1	641	5.9	1.9	11	6	10		90		4.5		87		13
	1/21, pH 1	685	5.8	1.9	12	10	10		90		5.1		92		8
	1/27, pH 4.5	669	5.9	1.9	12	7	11		89		6.1		89		11
	1/31, pH 1	845	5.5	1.8	19	6	13		87		5.4		88		12
	2/4, pH 1	615	6.0	1.9	6.5	5	6		94		14		86		14
	2/7, pH 1	654	5.9	1.9	7.0	10	7		93		12		94		6
	2/14, pH 1	643	5.9	1.9	8.4	9	8		92		17		91		9
	2/22, pH 1	487	6.5	2.1	8.5	10	10	> 99	90	< 1	7.4	< 1	94	> 99	6
	2/24, pH 1	469	6.6	2.1	11	7	14		86		21		90		10
CTC	1/21, pH 1	685	5.8	1.9	10	5	9		91		9.3		87		13
	1/21, pH 5	685	5.8	1.9	10	5	9		91		7.4		87		13
	2/7, pH 1	654	5.9	1.9	7.1	10	7		93		18		93		7
	2/14, pH 1	643	5.9	1.9	11	8.7	10		90		27		78		9
	2/22, pH 5	487	6.5	2.1	8.2	7	10		90		9.7		90		10
	2/24, pH 5	469	6.6	2.1	11	6	14		86		3.1		87		13

490

[a] $[O_2]$ in ALW was estimated using the temperature-corrected Henry's Law constant (Sander, 2023) and the composite-average Fairbanks temperature listed in Table S1.

[b] Rate of mass transport of gas-phase $\bullet OH$ to ambient water drops (where PME conditions are equivalent to a cloud/fog drop) or particles (ALW conditions), calculated using the parameters described in Tables S4 – S6. PME and ALW values are multiplied by 10^{10} and 10^7, respectively, to make them easier to display in the table. For example, the House 1/15 rates are 5.9×10^{-10} and 1.9×10^{-7} M s^{-1} for PME (cloud/fog) and ALW conditions, respectively.

[c] Pseudo-first-order rate constant for $\bullet OH$ loss due to reaction with DOC. PME and ALW values are multiplied by 10^{-5} and 10^{-9}, respectively; e.g., the House 1/15 rate constants are 11×10^5 and 6×10^9 s^{-1} for PME (cloud/fog) and ALW conditions, respectively.

Table S17 (a) and (b). Lifetimes of organic compounds due to reactions with (a) $^3C^*$ and $^•OH$ and (b) $^1O_2^*$ and $^•OH$.

Compound	Rate Constant (M⁻¹ s⁻¹) [a]		Lifetime of Compound [c]	
	$^3C^*$	$^•OH$	$^3C^*$ (hrs)	$^•OH$ (hrs)
Syringyl Acetone	4.5×10^9	1.4×10^{10}	0.074	9.1
Syringic Acid	3.2×10^9	9.4×10^9	0.10	14
Syringol	6.7×10^9	1.5×10^{10}	0.50	8.5
Guaiacyl Acetone	3.3×10^9	8.8×10^9	0.10	15
Guaicol	3.2×10^9	6.8×10^9	0.10	19
Ferulic Acid	3.4×10^9	1.3×10^{10}	0.098	9.8

Compound	Rate Constant (M⁻¹ s⁻¹) [b]		Lifetime of Compound [c]	
	$^1O_2^*$	$^•OH$	$^1O_2^*$ (hrs)	$^•OH$ (hrs)
Benzimidazole	2.5×10^6	7.9×10^9	12	16
Imidazole	4.0×10^7	6.4×10^9	0.75	20
Indole	4.5×10^7	1.4×10^{10}	0.67	9.3
Vanillin	4.6×10^{6} [d]	4.2×10^{9} [e]	6.6	30
Syringol	3.6×10^7	1.5×10^{10} [f]	0.84	8.5
4-Nitrophenol	2.5×10^6	4.1×10^9	12.1	31
Histidine	7.0×10^7	4.8×10^9	0.43	27
Tyrosine	8.0×10^6	1.3×10^{10}	3.8	9.8
Tryptophan	3.4×10^7	1.3×10^{10}	0.89	9.8
Methionine	1.6×10^7	7.4×10^9	1.9	17
Cysteine	8.3×10^6	1.9×10^{10}	3.6	6.7
Resorcinol	2.0×10^7	5.8×10^9	1.5	22
Hydroquinone	2.5×10^7	1.1×10^{10}	1.2	12
Niclosamide	2.3×10^7	7.5×10^9	1.3	17

[a] Rate constants reported by Ma et al. (2021) and Arciva et al. (2022) were measured at pH 2 and at 20 °C.
[b] Rate constants reported by Manfrin et al. (2019) unless otherwise noted.
[c] Lifetimes were determined using the average peak three-hour photooxidant concentrations from all House site samples; $[^3C^*] = 8.4\times10^{-13}$ M; $[^1O_2^*] = 9.2\times10^{-12}$ M; $[^•OH] = 2.2\times10^{-15}$ M.

[e] Manfrin et al. (2019) lists a $k_{vanillin+1O2*}$ of 3.6×10^5 M^{-1} s^{-1}, which was measured by Machado et al. (1997) in methanol and is an order of magnitude smaller than the 4.6×10^6 M^{-1} s^{-1} measured by Zhou et al., 2023) in water. We calculate the lifetime of vanillin with respect to $^1O_2*$ using the Zhou et al. (2023) value reported in the table.

510   [e] Manfrin et al. (2019) use an estimated $k_{vanillin+\bullet OH}$ of 4×10^8 M^{-1} s^{-1}, which is 10 times smaller than the rate constant for vanillyl alcohol and $^\bullet$OH at pH 2 measured by Arciva et al. (2022). Here, use the measured $k_{vanillyl\ alcohol+\bullet OH}$ of 8.2×10^9 M^{-1} s^{-1} reported by Arciva et al. (2022) as a proxy for the rate constant of vanillin with $^\bullet$OH.

[f] Manfrin et al. (2019) reported a $k_{syringol+\bullet OH}$ of 5.8×10^{10} M^{-1} s^{-1}, which is roughly four times higher than the rate constant at pH 2 measured by Smith et al. (2015).

Table S18. Kinetics and assumptions used to model secondary SO_4^{2-} Formation. All oxidants and oxidation pathways are aqueous unless noted otherwise.

Oxidant	Reaction Kinetics	Description & Assumptions	Reference
$^3C^*$	$k_{3C^*+S(IV)} = 1.3 \times 10^8$ M^{-1} s^{-1}	The rate constant listed here is assumed to be the same for all three inorganic S(IV) species: $SO_2 \cdot H_2O$, HSO_3^-, and SO_3^{2-}. The rate constant was not adjusted for temperature. The $^3C^*$ activity coefficient is assumed to be 1.	(Wang et al., 2020)
HOOH	$P_{SO42-} = P_{HOOH}$ (S19)	The production rate of SO_4^{2-} from HOOH is equal to the production rate of HOOH in the range of [inorganic S(IV)] predicted for Fairbanks particles (Sunday et al., 2024). The production rate was not adjusted for temperature. The HOOH activity coefficient is assumed to be 1.	(Anastasio et al., 1997; Sunday et al., 2024)
O_3	$log \dfrac{P_{measured}}{P_{predicted,I=0}} = a\left(\dfrac{\sqrt{I}}{1+\sqrt{I}}\right) + bI$ (S20) $a = 1.475(\pm 0.004)$ $b = 0.070(\pm 0.001)$ kg mol^{-1} $P_{aq,O_3} = \dfrac{P_{measured}}{P_{predicted,I=0}}\big(k_0[SO_2 \cdot H_2O] + k_1[HSO_3^-]$ $+ k_2[SO_3^{2-}]\big)$ (S21) $H_{O_3} = e^{\left(\frac{2297}{T} - 2.659 \times I_s + 688 \times \frac{I_s}{T} - 12.19\right)}$ (S22) $k_0 = 2.4 \times 10^4$ M^{-1} s^{-1} $k_1 = 3.7 \times 10^5$ M^{-1} s^{-1} $k_2 = 1.5 \times 10^9$ M^{-1} s^{-1}	Equations were determined by fitting experimentally determined ratios of S(IV) oxidation rates, $\dfrac{P_{measured}}{P_{predicted,I=0}}$, with ionic strengths between 2 and 14 mol kg^{-1} (Yu et al., 2023). [O_3] was predicted with the Henry's Law constant adjusted for temperature and ionic strength. The correction for ionic strength of the Henry's Law constant for ozone was validated only until $I_s = 0.6$ M but is used here until $I_s = 23$ M. The rate constant was not adjusted for temperature.	(Yu et al., 2023)
$TMI + O_2$	pH ≤ 4.2 $P_{SO_4^{2-}} = k_3[H^+]^{-0.74}[S(IV)][Mn(II)][Fe(III)]$ (S23) $k_3 = 3.72 \times 10^7 \times e^{(-8431.6 \times (\frac{1}{T} - 1/297))}$ M^{-2}s^{-1} (S24) pH > 4.2	The equation to correct the rate constants for ionic strength was determined for $I_s \leq 2$ M. We assume this relationship holds for the entire range of ionic strengths predicted for our particles (maximum $I_s = 23$ M). The activity coefficients (γ_{Is}) of metal species were determined using the equations listed here.	(Ibusuki and Takeuchi, 1986)

	$P_{SO_4^{2-}} = k_4[H^+]^{0.67}[S(IV)][Mn(II)][Fe(III)]$ (S25) $k_4 = 2.51 \times 10^{13} \times e^{(-8431.6 \times (\frac{1}{T} - 1/297))} \, M^{-2}s^{-1}$ (S26) $log_{10}\left(\frac{k}{k^{I_s=0}}\right) = \frac{-3.02\sqrt{I_s}}{1+\sqrt{I_s}}$ (S27) For Mn(II): $log_{10}(\gamma_{Is}) = \frac{-z_i^2 \times 0.5109 \sqrt{I_s}}{1+1.5 \times \sqrt{I_s}}$ (S28) For Fe(III), γ_{Is}= 0.001		(Martin & Hill, 1987) (Song et al., 2021)
Gas-phase $^\bullet$OH	$k(T) = \left(\frac{\frac{k_0(T)[M]}{1+\frac{k_0(T)[M]}{k_\infty(T)}}}{}\right)0.6^z$ (S29) $z = \left(1 + \left[log_{10}\left(\frac{k_0(T)[M]}{k_\infty(T)}\right)\right]^2\right)^{-1}$ (S30) $k_0(T) = k_0^{300}\left(\frac{T}{300}\right)^{-n}$ (S31) $k_\infty(T) = k_\infty^{300}\left(\frac{T}{300}\right)^{-m}$ (S32) [M] = concentration of N_2 and O_2 k_0^{300} = 3.3×10^{-31} cm^6 molecule^{-2} s^{-1} n = 4.3 k_∞^{300} = 1.6×10^{-12} cm^3 molecule^{-1} s^{-1} m = 0	[O$_2$] and [N$_2$] were determined assuming the ideal gas law applies and that O$_2$ and N$_2$ account for 21% and 78% of the gas molecules in the atmosphere.	(Cheng et al., 2016)
Aqueous-phase $^\bullet$OH	$k_{\bullet OH+HSO3-}$ = 4.5×10^9 M^{-1} s^{-1} (at 298 °K)	Seinfeld & Pandis (2016) report a multistep mechanism with 14 different rate constants. Here, we make two assumptions. First, we assume HSO$_3^-$ is the dominant inorganic S(IV) species and that its activity is equal to that of inorganic S(IV). Second, we assume the first step of the reaction is the rate-determining step, and therefore that $k_{\bullet OH+HSO3-}$ defines the rate of SO$_4^{2-}$ formation. The rate constant was not adjusted for temperature or ionic strength. The activity coefficient of $^\bullet$OH is assumed to be 1.	(Seinfeld & Pandis, 2016)

NO₂	$k_{NO2+S(IV)} = 1.4 \times 10^5 \text{ M}^{-1} \text{ s}^{-1} \text{ (pH < 5)}$ $P_{SO_4^{2-}} = k_{NO2+S(IV)}[S(IV)][NO_{2(aq)}] \quad (S33)$ $log_{10}\left(\frac{k}{k^{I_{s=0}}}\right) = cI_s \quad (S34)$ $c = 0.01$ $H_{NO_2}^{I_s=0} = 1.0 \times 10^{-2} \times e^{\left(2516.2 \times \left(\frac{1}{T} - \frac{1}{298}\right)\right)} \quad (S35)$	While several values of $k_{NO2+S(IV)}$ have been reported across a range of pH values, the value at pH < 5 is disputed. The reaction of NO_2 with S(IV) is highly pH dependent, with higher pHs associated with faster reactions with rate constants an order of magnitude higher than the $k_{NO2+S(IV)}$ reported here. However, Tilgner et al. (2021) explain that the fast rate constants measured in dilute solution are not likely to be relevant in the briny, high ionic strengths characteristic of aerosol liquid water. They report $k_{NO2+HSO3-}$ of 13 M^{-1} s^{-1} and $k_{NO2+SO3-2}$ of 270 M^{-1} s^{-1}. Here, we use $k_{NO2+S(IV)}$ at pH < 5 for both the low and high pH regimes. The rate constant was not adjusted for temperature. The activity coefficient of NO_2 was assumed to be equal to the activity coefficient of S(IV).	(Lee & Schwartz, 1982) (Clifton et al., 1988) (Cheng et al., 2016) (Seinfeld & Pandis, 2016)
HONO	pH < 4 $R_{SO_4^{2-}} = k_5[H^+]^{0.5}[N(III)][S(IV)] \quad (S36)$ $k_5 = 143 \text{ M}^{-3/2} \text{ s}^{-1}$ 3 < pH < 7 $R_{SO_4^{2-}} = k_6[H^+][N(III)][S(IV)] \quad (S37)$ $k_6 = 4800 \text{ M}^{-2} \text{ s}^{-1}$ $H_{HONO}^{I_s=0} = 49 \times e^{\left(\left(\frac{-9.5}{1.987 \times 10^{-3}}\right) \times \left(\frac{1}{298.15} - \frac{1}{T}\right)\right)} \quad (S38)$ $[N(III)] = [HONO] + [NO_2^{-}] = \frac{[HONO]}{\alpha_0} \quad (S39)$ $\alpha_0 = \frac{1}{1 + \frac{K_a}{[H^+]}} \quad (S40)$	[N(III)] is the total aqueous-phase concentration of HONO and NO_2^-, estimated using the temperature-corrected physical Henry's law constant converted to the effective constant using the mole fraction for nitrous acid (α_0). The rate constant was not adjusted for temperature or ionic strength. The activity coefficient of HONO was assumed to be equal to the activity coefficient of inorganic S(IV).	(Wang et al., 2020) (Seinfeld & Pandis, 2016)

Table S19. Composite-averaged, midday ALW oxidant concentrations and gas-phase concentrations used to model secondary sulfate formation

Oxidant [a]		Sample								
		1/15	1/21	1/27	1/31	2/4	2/7	2/14	2/22	2/24
$\bullet OH_g$ (mlc cm^{-3}) [b]		3×10^5								
SO_2 (ppb)		7.8	11	12	20.	8.5	3.8	7.3	5.2	8.6
HONO (ppb)		N/A	0.62	0.76	0.91	0.45	0.24	0.37	0.31	N/A
O_3	(ppb)	9.0	6.0	5.0	0.9	15.0	20.0	13.0	18.0	4.0
	(M)	N/A	6×10^{-11}	9×10^{-10}	1×10^{-9}	3×10^{-9}	3×10^{-9}	1×10^{-9}	3×10^{-10}	6×10^{-11}
$^3C^*$ (M) [c]		9×10^{-13}	2×10^{-13}	2×10^{-13}	3×10^{-12}	6×10^{-13}	1×10^{-12}	1×10^{-12}	3×10^{-13}	3×10^{-13}
NO_2 (M)		N/A	8×10^{-10}	1×10^{-9}	3×10^{-9}	1×10^{-9}	7×10^{-10}	1×10^{-9}	6×10^{-10}	9×10^{-10}
N(III) (M)	pH 1	N/A	5×10^{-7}	5×10^{-7}	1×10^{-6}	2×10^{-7}	1×10^{-7}	2×10^{-7}	9×10^{-8}	N/A
	pH 5	N/A	7×10^{-5}	8×10^{-5}	2×10^{-4}	3×10^{-5}	2×10^{-5}	3×10^{-5}	1×10^{-5}	N/A
$\bullet OH_{aq}$ (M) [d,e]	pH 1	2×10^{-15}	7×10^{-16}	4×10^{-16}	4×10^{-15}	8×10^{-16}	7×10^{-16}	2×10^{-16}	2×10^{-16}	3×10^{-16}
	pH 5	5×10^{-16}	2×10^{-16}	1×10^{-16}	1×10^{-15}	3×10^{-16}	2×10^{-16}	6×10^{-16}	5×10^{-16}	9×10^{-16}
Fe_{aq} {M} [f,g]	pH 1	N/A	5×10^{-5}	2×10^{-6}	5×10^{-5}	8×10^{-5}	5×10^{-5}	5×10^{-5}	1×10^{-5}	1×10^{-5}
	pH 5	N/A	7×10^{-6}	2×10^{-6}	1×10^{-5}	1×10^{-5}	3×10^{-6}	2×10^{-6}	3×10^{-7}	6×10^{-7}
Mn_{aq} {M} [f,h]	pH 1	N/A	1×10^{-4}	7×10^{-5}	1×10^{-4}	2×10^{-4}	2×10^{-4}	1×10^{-4}	6×10^{-5}	5×10^{-5}
	pH 5	N/A	9×10^{-5}	7×10^{-5}	9×10^{-5}	1×10^{-4}	2×10^{-4}	9×10^{-5}	3×10^{-5}	3×10^{-5}

[a] Concentrations of $^3C^*$ and $\bullet OH_{aq}$ represent the midday peak three hours of sunlight for each filter, averaged across all days in the composite. Concentrations of NO_2, O_3, and HONO are averaged over the entire time period of each composite, not just the peak daylight hours.

[b] The gas-phase $\bullet OH$ concentration is the predicted peak daytime concentration averaged over the campaign (Kuhn et al., in preparation). The subsequent rate of sulfate formation from gas-phase $\bullet OH$ is an upper-bound daytime value. The $\bullet OH$ concentration predicted in Fairbanks is higher than typically expected for northern latitude winter conditions due to the abundance of HONO, which is the dominant daytime gas-phase $\bullet OH$ source in Fairbanks (Kuhn et al., in preparation).

[c] The relative standard deviation for the predicted $^3C^*$ concentrations in ALW ranges from 45 to 74%.

[d] The secondary sulfate formation model is based on measurements in the House site extracts, which we only extracted in pH 1 solution. [$\bullet OH$] at pH 5 was estimated using $[\bullet OH]_{pH5} = [\bullet OH]_{pH1} \times 0.42$ based on the ratio $[\bullet OH]_{pH5}:[\bullet OH]_{pH1}$ determined in the CTC samples (Figure 5).

[e] The relative standard deviations for $\bullet OH$ concentrations in ALW at pH 1 and 5 range from 6 to 25%.

[f] Soluble metal concentrations were measured in dilute particle extracts (Sunday et al., 2024) prepared from separate filter squares extracted into pH 1 H_2SO_4 solution and into Milli-Q water to determine the pH 1 and 5 metal concentrations, respectively. The concentration of metals in ALW was determined by multiplying the measured concentrations in particle extracts by the concentration factor between extracts and ALW conditions (Table S15).

[g] The fraction of the total water-soluble Fe pool that is Fe(II) during daylight hours is estimated to be 80% (Deguillaume et al., 2004). We considered this in our calculations by multiplying the concentrations reported in the table by 0.2, the fraction of Fe(III) available for reaction during daylight hours. To calculate the activity of Fe, we use the activity coefficient of 0.001 reported by Song et al. (2021) for both Fe(III) and Fe(II).

540   [h] The fraction of the total water-soluble Mn pool that is Mn(II) during daylight hours is estimated to be 70% (Majestic et al., 2007). We considered this in our calculations by multiplying the concentrations reported in the table by 0.7, the fraction of Mn(II) available for reactions during daylight hours. To determine the activity of Mn, we calculated activity coefficients between 0.06 and 0.09 as described by Martin & Hill (1987).

545

Table S20. Secondary sulfate model components: ALWC, ionic strength, total SO_4^{2-}, fraction 2° SO_4^{2-}, HMS, & inorganic S(IV)

Sample	$PM_{2.5}$ (µg m⁻³) [a]	ALWC (µg m⁻³) [b]	Ionic Strength (I_s) (M) [b]	Total SO_4^{2-} (µg m⁻³) [c]	2° SO_4^{2-} (%) [d]	HMS (µg m⁻³) [e]	S(IV) Activity Coefficient (γ_{Is})	Measured [f] (µg m⁻³)	Measured [f] {M}	Henry's Law Predicted Activity {M} pH 1	Henry's Law Predicted Activity {M} pH 5	Model-Predicted Activity {M} [g] Low pH [h]	Model-Predicted Activity {M} [g] High pH [i]
1/15	7.5	9.4	13	N/A									
1/21	12.0	12	13	3.0	19	0.29	0.73	0.37	0.27	9×10^{-8}	6×10^{-5}	0.01	0.002
1/27	17.7	11	14	4.0	28	0.50	0.70	0.76	0.58	9×10^{-8}	1×10^{-4}	0.01	0.0005
1/31	26.1	16	15	6.5	23	1.2	0.77	1.4	0.85	2×10^{-7}	6×10^{-4}	0.07	0.02
2/4	8.6	4.9	23	3.3	36	0.42	0.52	0.47	0.61	8×10^{-8}	6×10^{-5}	0.006	0.001
2/7	4.3	1.9	18	1.2	53	0.039	0.62	0.035	0.14	2×10^{-8}	1×10^{-6}	0.003	0.0008
2/14	7.2	6.1	14	2.1	37	0.12	0.69	0.15	0.21	5×10^{-8}	1×10^{-5}	0.01	0.005
2/22	3.6	9.5	5	1.0	57	0.07	0.82	0.06	0.06	3×10^{-8}	2×10^{-6}	0.001	N/A
2/24	12.5	32	5	3.1	22	0.43	0.82	0.35	0.11	3×10^{-8}	2×10^{-5}	0.03	0.01

[a] $PM_{2.5}$ measured at the NCore site by the Alaska Department of Environmental conservation, https://www.epa.gov/outdoor-air-quality-data/download-daily-data.

[b] Aerosol liquid water content (ALWC) determined using the ISORROPIA model as outlined in Campbell et al. (2024), accounting for the uptake of water by inorganic and organic components.

[c] Total sulfate (i.e., primary and secondary) measured in bulk (PM_{10}) filter sample extracts.

[d] Percent of total sulfate that is secondary, as reported by (Moon et al., 2024) and averaged over each composite period.

[e] Mass concentration of hydroxymethanesulfonate (HMS) in PM_{10}. This was determined as the S(IV) signal in the ion chromatograph that remained after adding HOOH to the extraction solution, which removes inorganic S(IV) (Dingilian et al., 2024).

[f] The measured inorganic S(IV) atmospheric concentration (and ALW activity) were determined as the difference in bisulfite/sulfite determined by ion chromatography in two different extracts of the same filter: (1) extraction in purified water minus (2) extraction in water containing HOOH. It appears that labile organo-S(IV) species on the PM decompose to inorganic S(IV) during filter extraction, so these species also appear as inorganic S(IV) during this measurement (Dingilian et al., 2024). Values were converted from µg m⁻³ to molarity using the ALWC.

[g] The model-predicted activity of inorganic S(IV) is defined as the point where the fraction of secondary sulfate formed by HOOH in the model matches the measurements from Moon et al. (2024). They differ between high and low pH conditions because rates of secondary sulfate formation are pH dependent for several of the reactions included here.

[h] The "low pH" regime reflects calculations performed at pH 1.

[i] The "high pH" regime reflects calculations performed between pH 4 and 5.

Table S21. Daytime rates of secondary SO_4^{2-} formation ($\mu g\ m^{-3}\ hr^{-1}$) under high and low pH conditions

Conditions	Oxidant [a]	House Site Sample								
		1/15	1/21	1/27	1/31	2/4	2/7	2/14	2/22	2/24
Daytime, Low pH [b]	HOOH		0.088	0.051	0.49	0.077	0.077	0.18	0.053	0.22
	O_3		0.105	0.076	0.076	0.16	0.076	0.28	0.033	0.078
	$^{\bullet}OH_g$		0.054	0.054	0.098	0.054	0.018	0.054	0.054	0.054
	NO_2		0.023	0.017	0.12	0.0020	0.0010	0.021	0.0076	0.15
	$^3C^*$		0.0066	0.0020	0.096	0.0011	0.0020	0.020	0.0036	0.054
	$^{\bullet}OH_{aq}$		0.0015	2.9×10^{-4}	0.0098	0.0001	7.4×10^{-5}	0.0025	0.0015	0.036
	TMI		0.0016	1.4×10^{-5}	4.6×10^{-4}	3.0×10^{-4}	2.0×10^{-4}	0.0016	0.0013	0.029
	HONO		0.0028	0.0011	0.011	6.6×10^{-5}	4.1×10^{-5}	8.7×10^{-4}	2.4×10^{-4}	N/A
	Total Rate	N/A [d]	**0.28**	**0.20**	**0.91**	**0.29**	**0.17**	**0.56**	**0.15**	**0.56**
Daytime, High pH [c]	HOOH		0.035	0.021	0.20	0.031	0.036	0.071		0.087
	O_3		0.022	0.005	0.016	0.032	0.027	0.093		0.079
	$^{\bullet}OH_g$		0.054	0.054	0.098	0.054	0.018	0.054		0.054
	NO_2		7.5×10^{-4}	5.7×10^{-4}	0.029	1.7×10^{-4}	1.6×10^{-4}	0.0030		0.019
	$^3C^*$		2.2×10^{-4}	6.7×10^{-5}	0.023	9.6×10^{-5}	3.3×10^{-4}	0.0029	N/A [e]	0.0068
	$^{\bullet}OH_{aq}$		1.5×10^{-5}	4.4×10^{-6}	6.6×10^{-4}	2.7×10^{-6}	3.5×10^{-6}	9.9×10^{-5}		0.0013
	TMI		8.9×10^{-5}	7.2×10^{-6}	3.9×10^{-4}	3.7×10^{-5}	1.9×10^{-5}	1.1×10^{-4}		0.0011
	HONO		9.6×10^{-6}	3.9×10^{-6}	2.7×10^{-4}	5.9×10^{-7}	7.1×10^{-7}	1.3×10^{-5}		N/A
	Total Rate		**0.11**	**0.080**	**0.36**	**0.12**	**0.082**	**0.23**		**0.24**

[a] HOOH, $^3C^*$, and $^{\bullet}OH_{aq}$ formation rates, and TMI concentrations, reflect measurements made on filter samples from the House site.
[b] The "low pH" regime reflects calculations performed at pH 1.
[c] The "high pH" regime reflects calculations performed between pH 4 and 5.
[d] Calculations could not be run for the 1/15 composite period since there were no actinic flux measurements.
[e] For the 2/22 High pH daytime composite, no valid model results were obtained because even at very low {inorganic S(IV)}, the maximum modelled fraction of secondary SO_4^{2-} produced by HOOH is smaller than the measured fraction reported by Moon et al. (2024).

Table S22. Parameters for modelling monthly average actinic fluxes with TUV

Date	Snow on the Ground?	Albedo [a]	Solar Noon [b]	Solar Zenith Angle at Solar Noon [b]
6/15/2021	No	0.1	13:51	41.5
7/15/2021	No	0.1	13:56	43.5
8/15/2021	No	0.1	13:55	51.1
9/15/2021	No	0.1	13:45	62.1
10/15/2021	No	0.1	13:36	73.6
11/15/2021	Slight	0.3	12:35	83.4
12/15/2021	Yes	0.85	12:46	87.9
1/15/2022	Yes	0.85	13:00	85.7
2/15/2022	Yes	0.85	13:04	77.2
3/15/2022	Yes	0.85	13:59	66.7
4/15/2022	Yes	0.4	13:50	54.8
5/15/2022	No	0.1	13:47	45.8
6/15/2022	No	0.1	13:51	41.5

575

[a] Wintertime albedo estimated based on upwelling-to-downwelling j_{NO2} measured during ALPACA and adjusted year-round based on snow cover.
[b] Determined from https://www.timeanddate.com/sun/usa/fairbanks?month=2&year=2022.

580

Table S23 a). Estimating O(^{1}D) loss pathways and production rates of $^\bullet$OH(g) from ozone photolysis ($P_{O3\rightarrow\bullet OH}$)

Month-Year	Average Temperature (°C)	Average Relative Humidity (%)	H$_2$O Saturation Vapor Pressure (mbar)	[H$_2$O(g)] (mlc cm^{-3})	$P_{O3\rightarrow\bullet OH}$ (mlc cm^{-3} s^{-1})
Jun-21	18	56	21	2.9×10^{17}	2.2×10^6
Jul-21	18	59	21	3.0×10^{17}	1.9×10^6
Aug-21	13	80	15	3.0×10^{17}	9.3×10^5
Sep-21	6.0	74	9.4	1.8×10^{17}	1.9×10^5
Oct-21	-1.5	86	5.5	1.3×10^{17}	2.7×10^4
Nov-21	-17	79	1.6	3.6×10^{16}	2.1×10^3
Dec-21	-17	82	1.6	3.7×10^{16}	1.8×10^3
Jan-22	-20	77	1.2	2.7×10^{16}	1.5×10^3
Feb-22	-17	79	1.6	3.6×10^{16}	2.3×10^4
Mar-22	-6.9	64	3.6	6.4×10^{16}	2.5×10^5
Apr-22	-0.90	49	5.7	7.4×10^{16}	6.3×10^5
May-22	11	50	13	1.6×10^{17}	1.4×10^6
Jun-22	17	49	20	2.4×10^{17}	2.6×10^6

Table S23 b). Estimated monthly photochemical rate constants for O_3, HONO, and BrC in Fairbanks. Values were calculated for midday on the 15th day of each month.

Month-Year	$j_{BrC \to 3C^*}$ (s^{-1})	$j_{O3 \to O(1D)}$ (s^{-1})	$j_{O3 \to \bullet OH}$ (s^{-1})	$j_{HONO \to \bullet OH}$ (s^{-1})
Jun-21	3.1×10^{-4}	2.3×10^{-5}	3.0×10^{-6}	1.5×10^{-3}
Jul-21	3.0×10^{-4}	2.2×10^{-5}	2.9×10^{-6}	1.4×10^{-3}
Aug-21	2.6×10^{-4}	1.5×10^{-5}	2.0×10^{-6}	1.2×10^{-3}
Sep-21	1.9×10^{-4}	6.6×10^{-6}	5.3×10^{-7}	9.0×10^{-4}
Oct-21	1.0×10^{-4}	1.7×10^{-6}	9.2×10^{-8}	4.6×10^{-4}
Nov-21	3.6×10^{-5}	3.6×10^{-7}	5.4×10^{-9}	1.7×10^{-4}
Dec-21	2.2×10^{-5}	2.1×10^{-7}	3.2×10^{-9}	1.1×10^{-4}
Jan-22	4.0×10^{-5}	4.2×10^{-7}	4.6×10^{-9}	2.1×10^{-4}
Feb-22	1.5×10^{-4}	2.5×10^{-6}	3.8×10^{-8}	7.5×10^{-4}
Mar-22	3.5×10^{-4}	1.1×10^{-5}	3.0×10^{-7}	1.7×10^{-3}
Apr-22	3.5×10^{-4}	1.8×10^{-5}	5.8×10^{-7}	1.7×10^{-3}
May-22	2.9×10^{-4}	1.9×10^{-5}	1.4×10^{-6}	1.4×10^{-3}
Jun-22	3.1×10^{-4}	2.3×10^{-5}	2.6×10^{-6}	1.5×10^{-3}

590
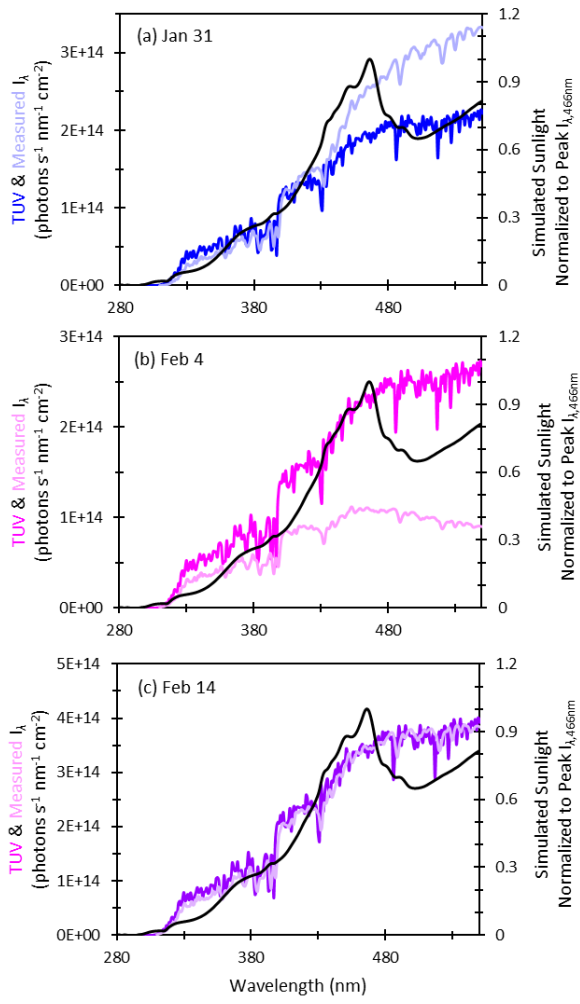
Figure S1. Comparison of laboratory, field, and modeled photon fluxes (I_λ) on (a) January 31st, (b) February 4th, and (c)
February 14th. The dark colored lines are modelled total actinic flux from TUV solar noon on each specified day and the light
colored lines are the total actinic flux measured on each specified day in Fairbanks, AK at 13:30, near solar noon. Both
measurements and modeled results are total actinic flux, i.e., the sum of upwelling and downwelling. The black line
represents the normalized photon fluxes of laboratory simulated sunlight. TUV data is from
https://www.acom.ucar.edu/Models/TUV/Interactive_TUV/.

600
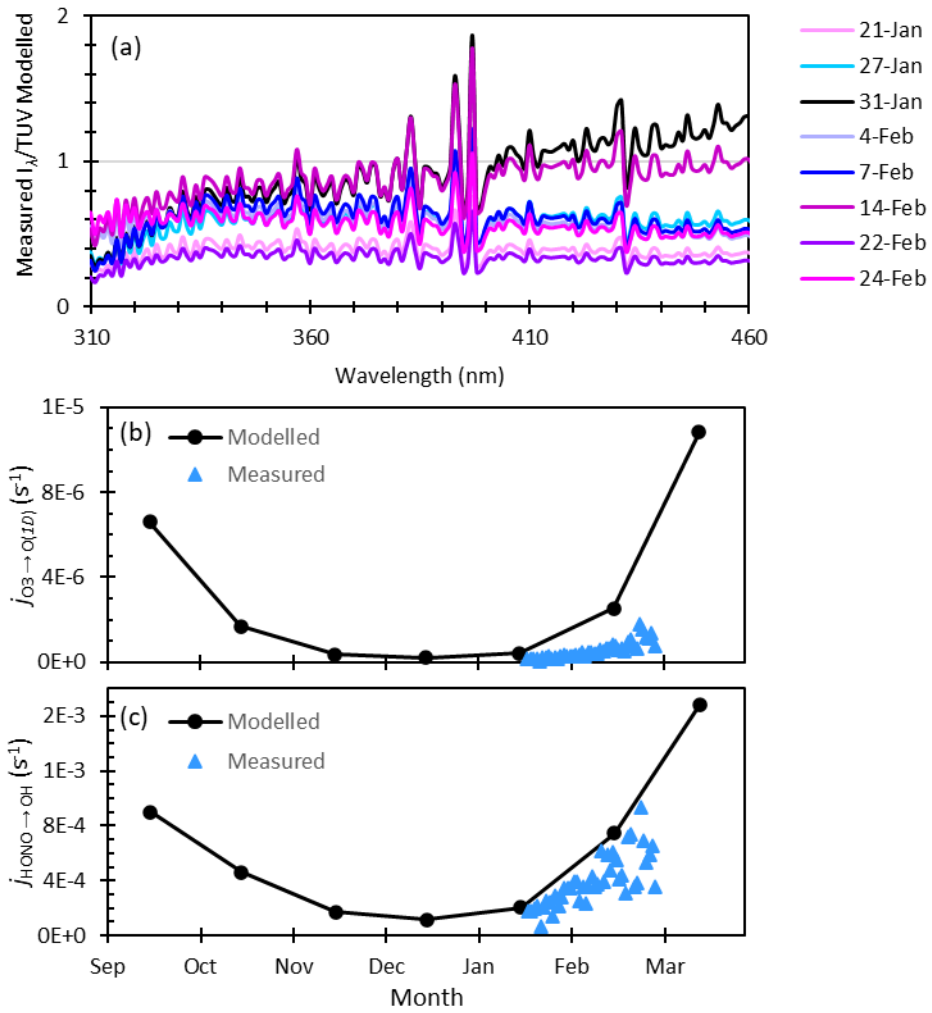
Figure S2. Comparison of modelled and measured actinic fluxes (I_λ) and photochemical rate constants (j). (a) Ratio of modelled (TUV) and measured actinic fluxes at midday on each composite midpoint date. (b) Rate constants for ozone photolysis ($j_{O3\to O(1D)}$) and (c) rate constants for photolysis of HONO ($j_{HONO\to \bullet OH}$) on the 15th day of each month.

605
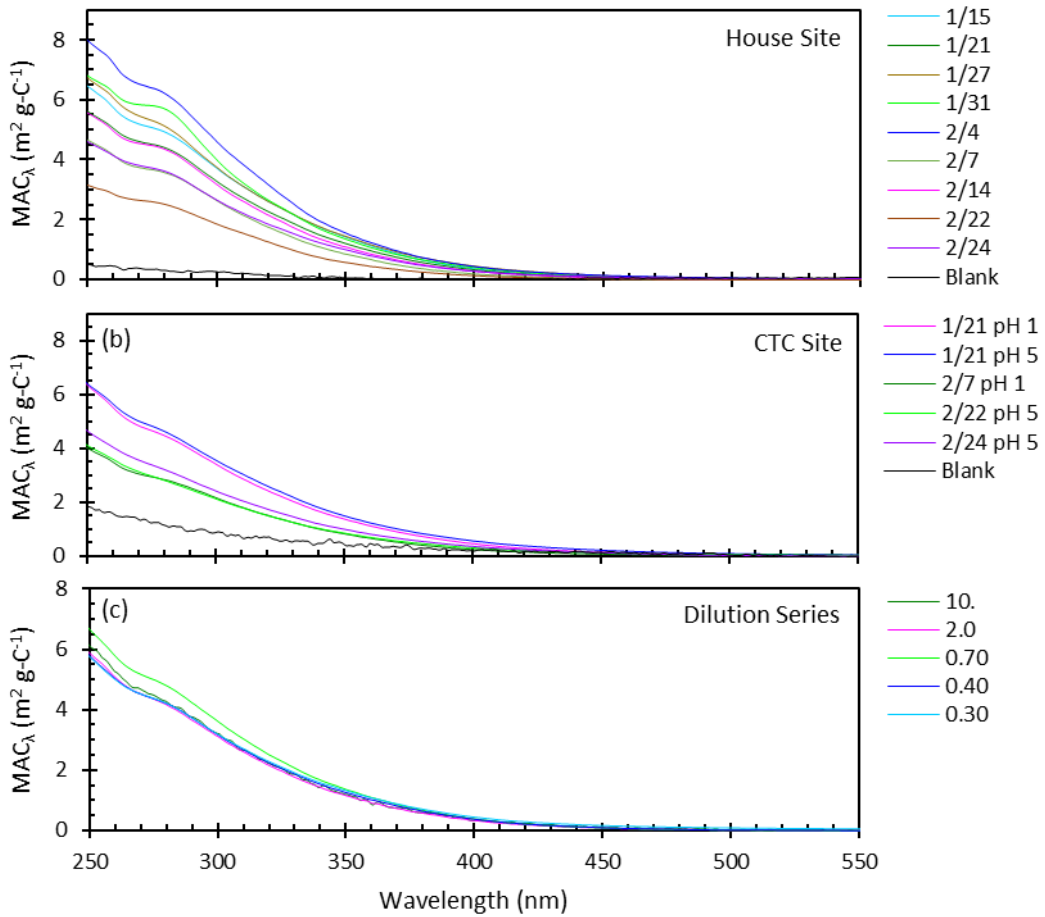
Figure S3. Spectrally resolved mass absorption coefficients of particle extracts at (a) the House site, (b) the CTC site, and (c) in the dilution series of the 2/14 CTC sample. In panel (c), each legend number represents the volume of H_2SO_4 solution used to extract each filter square for that dilution. While absorbance values at wavelengths above 500 nm look minimal, these wavelengths contribute to BrC photochemistry under Fairbanks sunlight.

615
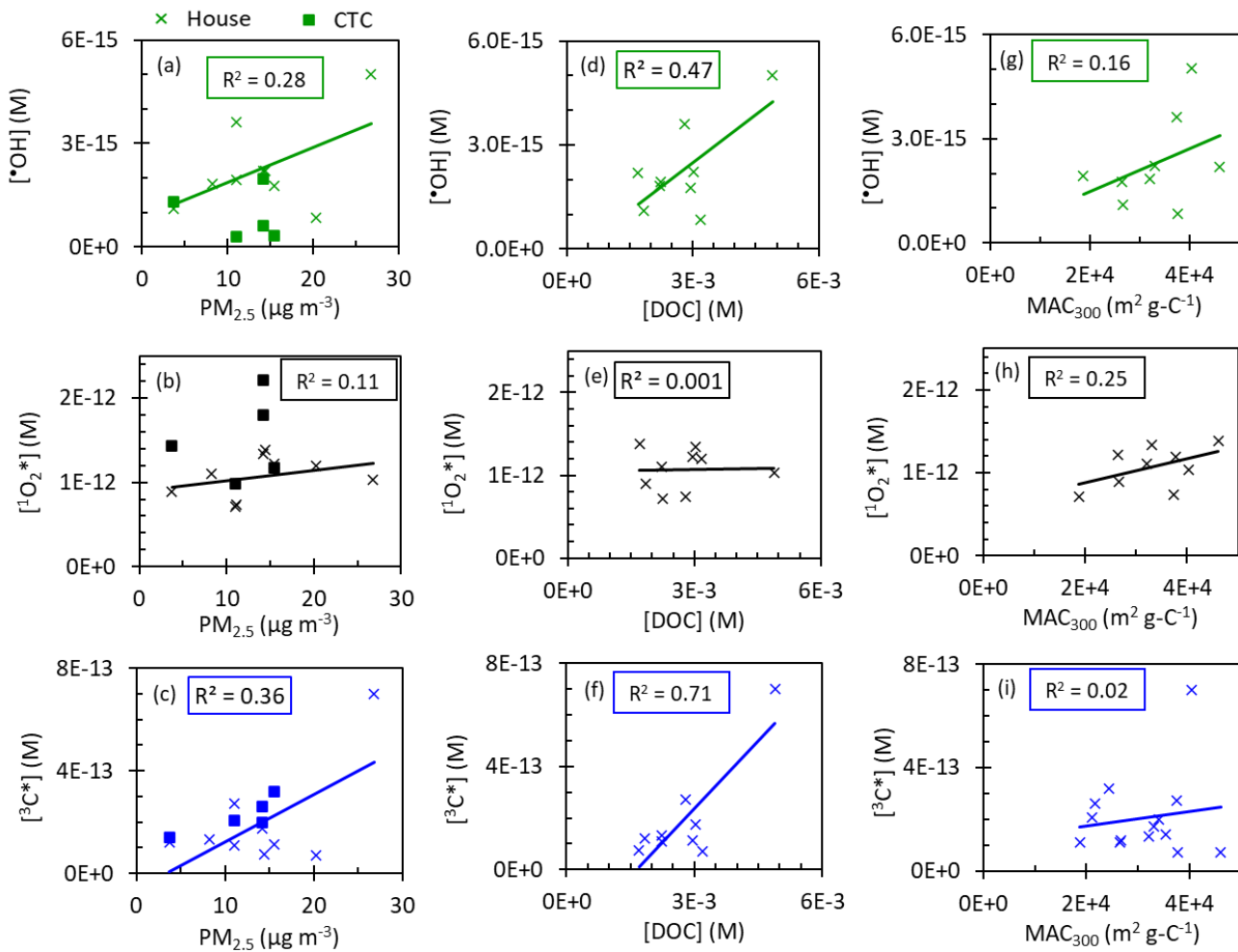
Figure S4. Correlations of •OH, $^1O_2$*, and ^3C* concentrations with $PM_{2.5}$, $[DOC]_{PME}$, and MAC_{300}. (a) – (c) all depict House (marked with 'x') and CTC site samples (marked with filled squares), while (d) – (i) only show House site samples. The regressions were calculated using only the House site samples to control for site differences. $[DOC]_{PME}$ at the House and CTC sites cannot be compared because the filters at the two sites collected different size bins, with the House site representing $PM_{2.5}$ and the CTC site representing $PM_{0.7}$.

620
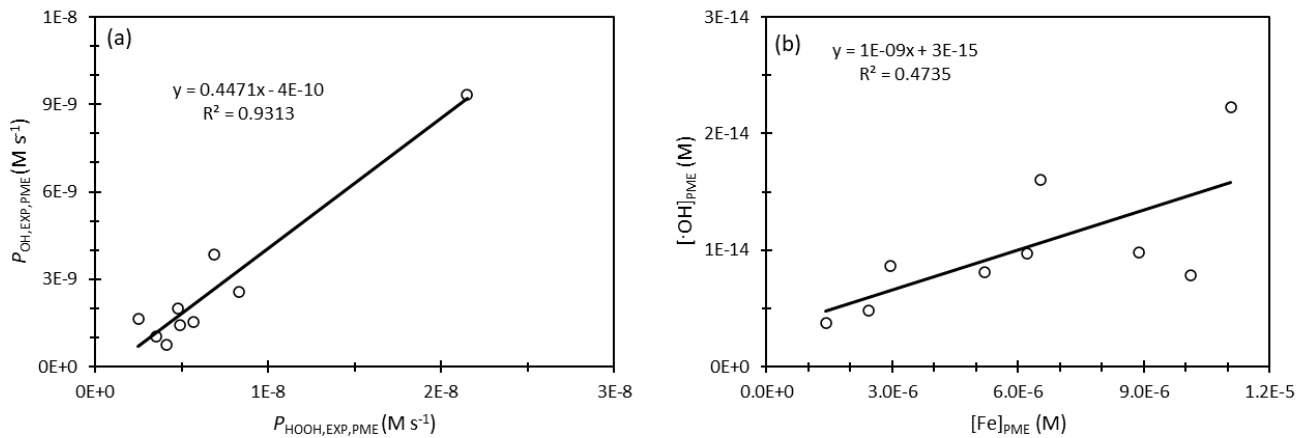
Figure S5. Correlations exploring •OH sources. (a) $P_{•OH,EXP,PME}$ versus $P_{HOOH,EXP,PME}$. (b) •OH concentration versus soluble Fe concentrations in pH 1 extracts.

625
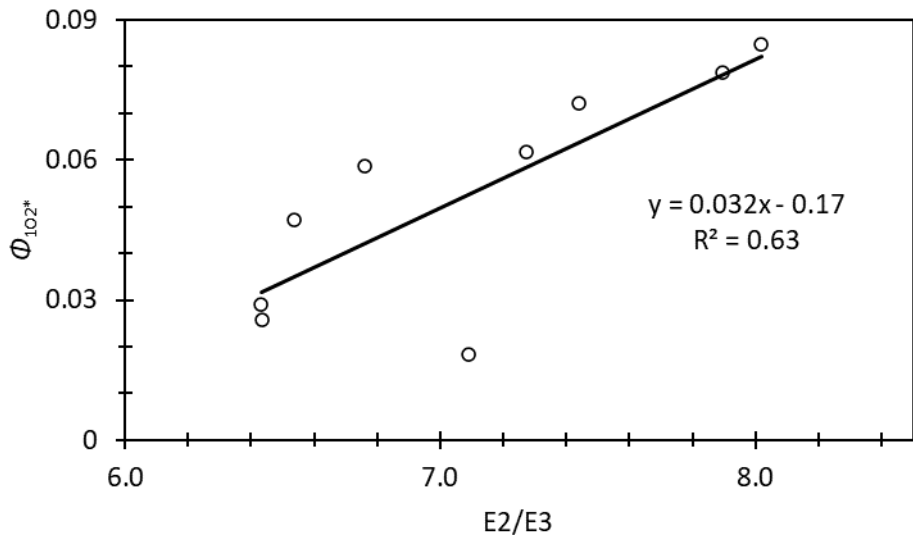
Figure S6. Relationship of Φ_{1O2*} and E2/E3.
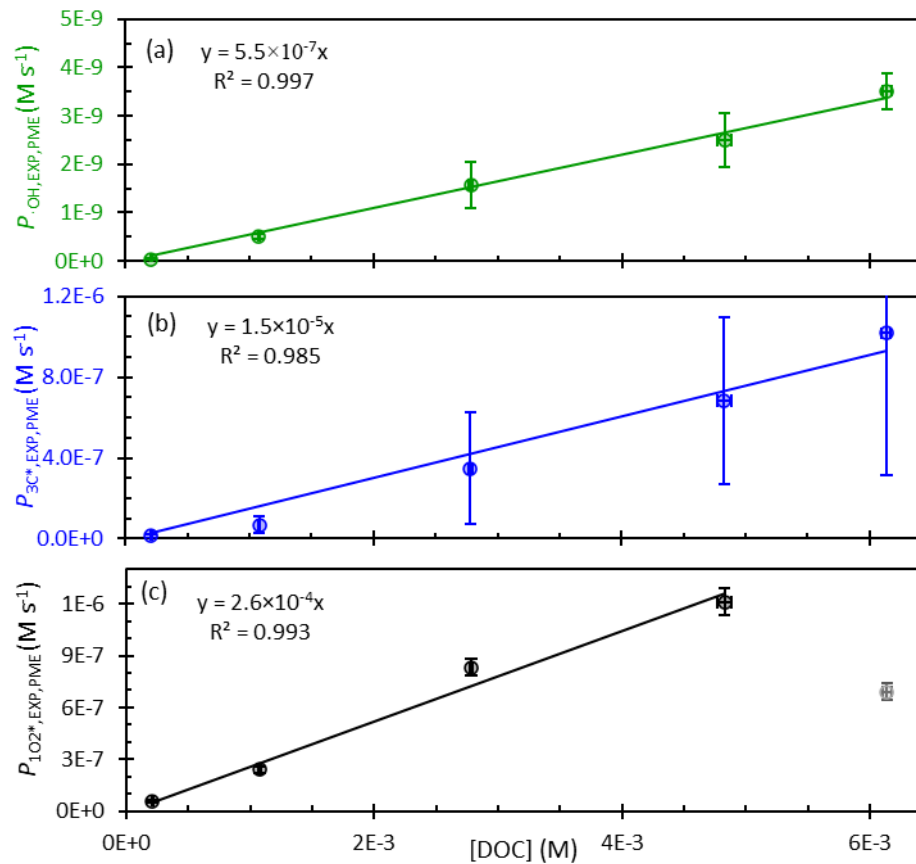
630

Figure S7. Formation rates from the dilution series for CTC sample 2/14 for (a) $^{\bullet}OH$, (b) $^3C^*$, and (c) $^1O_2^*$ as a function of [DOC]$_{PME}$. Formation rates are normalized to the average midday actinic flux on February 1st in Fairbanks (equivalent to $j_{2NB,AK}$ = 0.0045 s^{-1}). Solid lines represent linear regression fits to the experimental data. For panel (c), the point corresponding to the $^1O_2^*$ production rate at the highest DOC is not included in the regression.

635
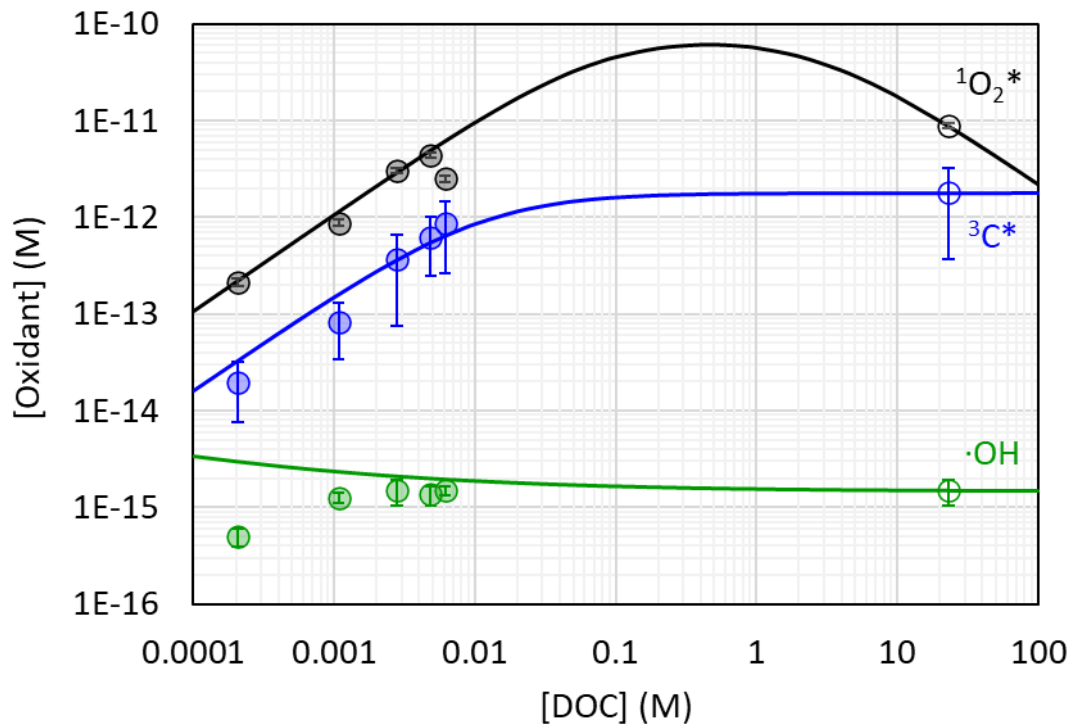
Figure S8. Extrapolation of photooxidant concentrations from dilute PM extracts to aerosol liquid water conditions for CTC sample 2/14 for singlet oxygen (gray circles), oxidizing triplets (blue circles) and hydroxyl radical (green circles). The filled circles at low DOC concentrations represent the dilution series measurements and the open circles at high DOC correspond to extrapolated values under ALW conditions, corresponding to an ALW PM-mass/H_2O-mass ratio of 0.69 µg-PM/µg-H_2O determined for the 2/14 CTC sample. Oxidant concentrations in the dilution series and ALW extrapolation were normalized to $j_{2NB,AK} = 0.0045$ s^{-1}, which corresponds to the average midday actinic flux for February 1st and includes the 2.5 enhancement factor due to optical confinement. Lines represent extrapolations, which were made using equations 4, 5, and 6 with parameters from Tables S14, S15, and S16. The line for •OH includes mass transport of •OH from the gas phase, which is why the green line is above the PM extract data points.
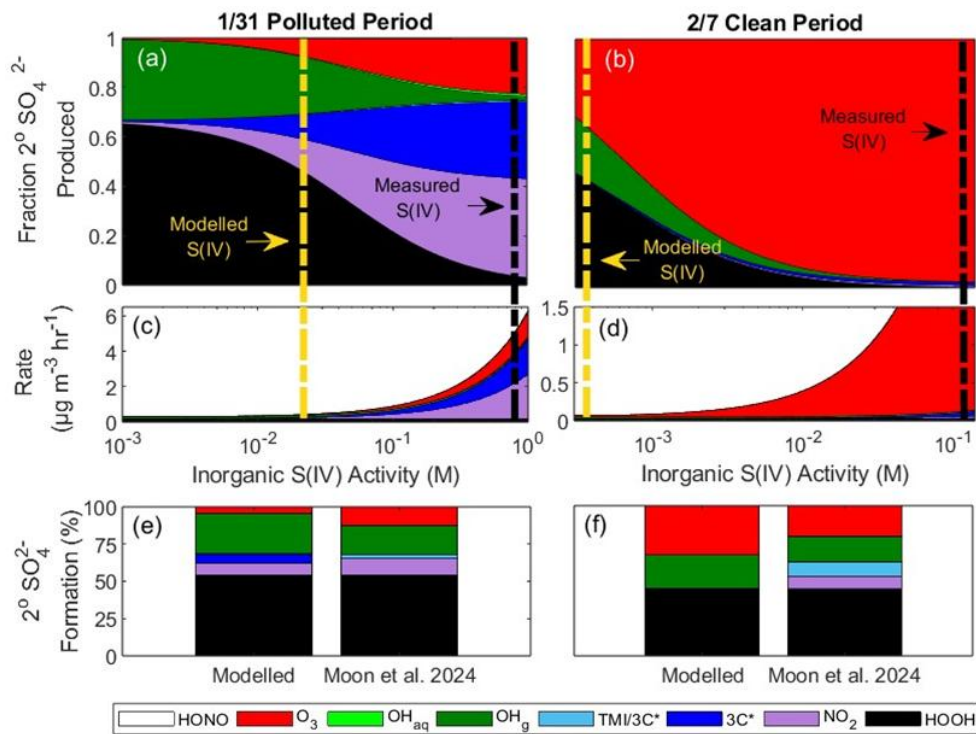
Figure S9. Modelled secondary (2°) SO_4^{2-} formation under high pH (pH 4-5), daytime conditions during the 1/31 polluted period and 2/7 clean period due to HOOH, NO_2, $^3C^*$, O_2 catalyzed by transition metal ions (TMI), gas-phase $^\bullet OH$, aqueous-phase $^\bullet OH$, and O_3. Panels (a) and (b) show the fraction of secondary SO_4^{2-} formation from the different oxidation pathways as a function of the activity of particle inorganic S(IV), i.e., sulfite and bisulfite. The black vertical dashed lines are the ALW inorganic S(IV) activities based on PM measurements, assuming all the HOOH-labile S(IV) is inorganic. The yellow vertical dashed lines are the ALW inorganic S(IV) activities at which our modelled fractions of secondary sulfate from HOOH match the fractions determined from isotopic measurements (Moon et al., 2024). Panels (c) and (d) show the total rate of secondary SO_4^{2-} formation from all pathways. Panels (e) and (f) show the percent contribution of each oxidant to secondary SO_4^{2-} formation at the modelled concentrations of inorganic S(IV) and the corresponding isotope-determined oxidant contributions from Moon et al. (2024). In our model results, sulfate formation from TMI is too small to see.
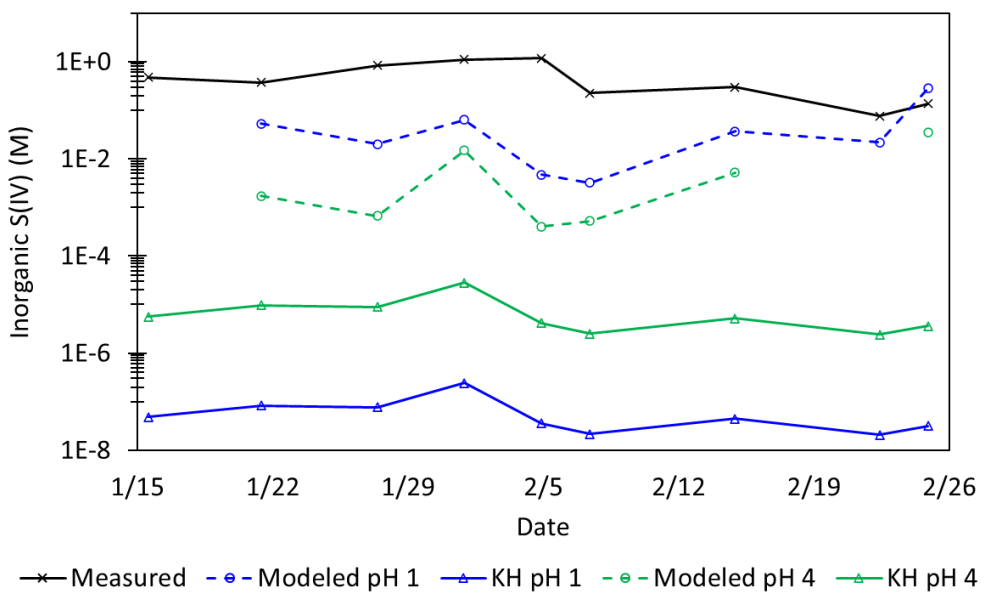
660

Figure S10. Inorganic S(IV) concentrations comparing measurements (black line), model results (dashed blue (pH 1) and green (pH 4) lines), and predictions from Henry's Law (K_H; solid blue (pH 1) and green (pH 4) lines). The measured values are likely overestimates because they probably include contributions from labile organo-S(IV) complexes that broke down to inorganic S(IV) when the filters were extracted.

References

Air Quality Monitoring Data: https://www.epa.gov/outdoor-air-quality-data/download-daily-data, last access: 10 November 2024.

Anastasio, C. and McGregor, K. G.: Chemistry of fog waters in California's Central Valley: 1. In situ photoformation of hydroxyl radical and singlet molecular oxygen, Atmos Environ, 35, 1079–1089, https://doi.org/10.1016/S1352-2310(00)00281-8, 2001.

Anastasio, C., Faust, B. C., and Rao, C. J.: Aromatic Carbonyl Compounds as Aqueous-Phase Photochemical Sources of Hydrogen Peroxide in Acidic Sulfate Aerosols, Fogs, and Clouds. 1. Non-Phenolic Methoxybenzaldehydes and Methoxyacetophenones with Reductants (Phenols), Environ Sci Technol, 31, 218–232, https://doi.org/https://doi.org/10.1021/es960359g, 1997.

Appiani, E., Ossola, R., Latch, D. E., Erickson, P. R., and McNeill, K.: Aqueous singlet oxygen reaction kinetics of furfuryl alcohol: Effect of temperature, pH, and salt content, Environ Sci Process Impacts, 19, 507–516, https://doi.org/10.1039/c6em00646a, 2017.

Arakaki, T., Anastasio, C., Kuroki, Y., Nakajima, H., Okada, K., Kotani, Y., Handa, D., Azechi, S., Kimura, T., Tsuhako, A., and Miyagi, Y.: A General Scavenging Rate Constant for Reaction of Hydroxyl Radical with Organic Carbon in Atmospheric Waters, Environ Sci Technol, 47, 8196–8203, https://doi.org/10.1021/es401927b, 2013.

Arciva, S., Niedek, C., Mavis, C., Yoon, M., Sanchez, M. E., Zhang, Q., and Anastasio, C.: Aqueous ·OH Oxidation of Highly Substituted Phenols as a Source of Secondary Organic Aerosol, Environ Sci Technol, 56, 9959–9967, https://doi.org/10.1021/acs.est.2c02225, 2022.

Ashton, L., Buxton, G. V, and Stuart, C. R.: Temperature Dependence of the Rate of Reaction of OH with Some Aromatic Compounds in Aqueous Solution Evidence for the Formation of a n-Complex Intermediate?, Journal of the Chemical Society, Faraday Transactions, 1631–1633, 1995.

Bogler, S., Daellenbach, K. R., Bell, D. M., Prévôt, A. S. H., El Haddad, I., and Borduas-Dedekind, N.: Singlet Oxygen Seasonality in Aqueous PM_{10} is Driven by Biomass Burning and Anthropogenic Secondary Organic Aerosol, Environ Sci Technol, 56, 15389–15397, https://doi.org/10.1021/acs.est.2c04554, 2022.

Cheng, Y., Zheng, G., Wei, C., Mu, Q., Zheng, B., Wang, Z., Gao, M., Zhang, Q., He, K., Carmichael, G., Pöschl, U., and Su, H.: Reactive nitrogen chemistry in aerosol water as a source of sulfate during haze events in China, Sci Adv, 2, https://doi.org/DOI: 10.1126/sciadv.1601530, 2016.

Clifton, C. L., Altstein, M., and Hule, R. E.: Rate Constant for the Reaction of NO_2 with Sulfur(IV) over the pH Range of 5.3-13, Environ. Sci. Technol, 22, 586–589, https://doi.org/https://doi.org/10.1021/es00170a018, 1988.

Deguillaume, L., Leriche, M., Monod, A., and Chaumerliac, N.: The role of transition metal ions on HOx radicals in clouds: a numerical evaluation of its impact on multiphase chemistry, Atmos. Chem. Phys, 4, 95–110, https://doi.org/https://doi.org/10.5194/acp-4-95-2004, 2004.

Dingilian, K., Hebert, E., Battaglia, M., Campbell, J. R., Cesler-Maloney, M., Simpson, W., St. Clair, J. M., Dibb, J., Temime-Roussel, B., D'Anna, B., Moon, A., Alexander, B., Yang, Y., Nenes, A., Mao, J., and Weber, R. J.: Hydroxymethanesulfonate and Sulfur(IV) in Fairbanks Winter During the ALPACA Study, ACS ES&T Air, 1, 646–659, https://doi.org/10.1021/acsestair.4c00012, 2024.

Edwards, K. C., Kapur, S., Fang, T., Cesler-Maloney, M., Yang, Y., Holen, A. L., Wu, J., Robinson, E. S., DeCarlo, P. F., Pratt, K. A., Weber, R. J., Simpson, W. R., and Shiraiwa, M.: Residential Wood Burning and Vehicle Emissions as Major Sources of Environmentally Persistent Free Radicals in Fairbanks, Alaska, Environ Sci Technol, https://doi.org/10.1021/acs.est.4c01206, 2024.

Haag, W. R. and Hoigne, J.: Siglet Oxygen in Surface Waters. 3. Photochemical Formation and Steady-State Concentrations in Various Types of Waters, J. Environ. Sci. Technol, 20, 341–348, https://doi.org/doi.org/10.1021/es00146a005, 1986.

Helms, J. R., Stubbins, A., Ritchie, J. D., Minor, E. C., Kieber, D. J., and Mopper, K.: Absorption spectral slopes and slope ratios as indicators of molecular weight, source, and photobleaching of chromophoric dissolved organic matter, Limnol Oceanogr, 53, 955–969, https://doi.org/10.4319/lo.2008.53.3.0955, 2008.

Hullar, T., Bononi, F. C., Chen, Z., Magadia, D., Palmer, O., Tran, T., Rocca, D., Andreussi, O., Donadio, D., and Anastasio, C.: Photodecay of guaiacol is faster in ice, and even more rapid on ice, than in aqueous solution, Environ Sci Process Impacts, 22, 1666–1677, https://doi.org/10.1039/d0em00242a, 2020.

Ibusuki, T. and Takeuchi, K.: Sulfur dioxide oxidation by oxygen catalyzed by mixtures of manganese(II) and iron(III) in aqueous solutions at environmental reaction conditions, Atmos Environ, 21, 1555–1560, https://doi.org/https://doi.org/10.1016/0004-6981(87)90317-9, 1986.

Kaur, R., Labins, J. R., Helbock, S. S., Jiang, W., Bein, K. J., Zhang, Q., and Anastasio, C.: Photooxidants from brown carbon and other chromophores in illuminated particle extracts, Atmos Chem Phys, 19, 6579–6594, https://doi.org/10.5194/acp-19-6579-2019, 2019.

Kim, S., Vandenboer, T. C., Young, C. J., Riedel, T. P., Thornton, J. A., Swarthout, B., Sive, B., Lerner, B., Gilman, J., Warneke, C., Roberts, J. M., Guenther, A., Wagner, N. L., Dubé, W. P., Williams, E., and Brown, S. S.: The primary and recycling sources of OH during the NACHTT-2011 campaign: HONO as an important OH primary source in the wintertime, J Geophys Res, 119, 6886–6896, https://doi.org/10.1002/2013JD019784, 2014.

Kuhn, J., Heinlein, L. M. D., Cesler-Maloney, M., Stutz, J., Anastasio, C., Simpson, W., Dibb, J., Jennie, T., Bartels-Rausch, T., Sunday, M. O., Guo, F., Flynn III, J. H., and Fahey, K.: Oxidation in Polluted Surface Layers During High-Latitude Winter, Atmos Chem Phys, n.d.

Lee, Y. and Schwartz, S. E.: Kinetics of oxidation of aqueous sulfur (IV) by nitrogen dioxide, Precipitation Scavenging, Dry Deposition and Resuspension, 1, 453–470, 1983.

Ma, L., Guzman, C., Niedek, C., Tran, T., Zhang, Q., and Anastasio, C.: Kinetics and Mass Yields of Aqueous Secondary Organic Aerosol from Highly Substituted Phenols Reacting with a Triplet Excited State, Environ Sci Technol, 55, 5772–5781, https://doi.org/10.1021/acs.est.1c00575, 2021.

Ma, L., Worland, R., Tran, T., and Anastasio, C.: Evaluation of Probes to Measure Oxidizing Organic Triplet Excited States in Aerosol Liquid Water, Environ Sci Technol, 57, 6052–6062, https://doi.org/10.1021/acs.est.2c09672, 2022.

Ma, L., Worland, R., Jiang, W., Niedek, C., Guzman, C., Bein, K. J., Zhang, Q., and Anastasio, C.: Predicting photooxidant concentrations in aerosol liquid water based on laboratory extracts of ambient particles, Atmos Chem Phys, 23, 8805–8821, https://doi.org/10.5194/acp-23-8805-2023, 2023.

Ma, L., Worland, R., Heinlein, L., Guzman, C., Jiang, W., Niedek, C., Bein, K. J., Zhang, Q., and Anastasio, C.: Seasonal variations in photooxidant formation and light absorption in aqueous extracts of ambient particles, Atmos Chem Phys, 24, 1–21, https://doi.org/10.5194/acp-24-1-2024, 2024.

Machado, A. E. H., Gomes, A. J., Campos, C. M. F., Terrones, M. G. H., Perez, D. S., Ruggiero, R., and Castellan, A.: Photoreactivity of lignin model compounds in the photobleaching of chemical pulps 2. Study of the degradation of 4-hydroxy-3-methoxy-benzaldehyde and two lignin fragments induced by singlet oxygen, 1997.

Madronich, S. and Flocke, S.: The role of solar radiation in atmospheric chemistry, in: Handbook of Environmental Chemistry, Springer-Verlag, 1–26, 1998.

Majestic, B. J., Schauer, J. J., and Shafer, M. M.: Development of a manganese speciation method for atmospheric aerosols in biologically and environmentally relevant fluids, Aerosol Science and Technology, 41, 925–933, https://doi.org/10.1080/02786820701564657, 2007.

Martin, L. R. and Hill, M. W.: The Effect of Ionic Strength on the Manganese Catalyzed Oxidation of Sulfur (IV), Atmos Environ, 21, 2267–2270, https://doi.org/https://doi.org/10.1016/0004-6981(87)90361-1, 1987.

McNeill, K. and Canonica, S.: Triplet state dissolved organic matter in aquatic photochemistry: Reaction mechanisms, substrate scope, and photophysical properties, Environ Sci Process Impacts, 18, 1381–1399, https://doi.org/10.1039/c6em00408c, 2016.

Millero, F., Hershey, J. P., Johnson, G., and Zhang, J.-Z.: The Solubility of SO_2 and the Dissociation of H_2SO_3 in NaCl Solutions, J Atmos Chem, 8, 377–389, https://doi.org/https://doi.org/10.1007/BF00052711, 1989.

Moon, A., Jongebloed, U., Dingilian, K. K., Schauer, A. J., Chan, Y.-C., Cesler-Maloney, M., Simpson, W. R., Weber, R. J., Tsiang, L., Yazbeck, F., Zhai, S., Wedum, A., Turner, A. J., Albertin, S., Bekki, S., Savarino, J., Gribanov, K., Pratt, K. A., Costa, E. J., Anastasio, C., Sunday, M. O., Heinlein, L. M. D., Mao, J., and Alexander, B.: Primary Sulfate Is the Dominant Source of Particulate Sulfate during Winter in Fairbanks, Alaska, ES&T Air, 1, 139–149, https://doi.org/10.1021/acsestair.3c00023, 2024.

AK Fairbanks 11 NE: https://erddap.aoos.org/erddap/tabledap/ncei-uscrn-ak_fairbanks_11_ne-v2.html, last access: 10 November 2024.

Peuravuori, J. and Pihlaja, K.: Molecular size distribution and spectroscopic properties of aquatic humic substances, Anal Chim Acta, 337, 133–149, 1997.

Ross, A. B., Mallard, W. G., Helman, W. P., Buxton, G. V., Huie, R., and Neta, E. P.: NDRL-NIST Solution Kinetics Database - Version 2, Gaithersburg, MD, 1994.

Ross, F. and Ross, A. B.: Selected specific rates of reactions of transients from water in aqueous solution, Gaithersburg, MD, https://doi.org/10.6028/NBS.NSRDS.59, 1977.

Sander, R.: Compilation of Henry's law constants (version 5.0.0) for water as solvent, https://doi.org/10.5194/acp-23-10901-2023, 6 October 2023.

770 Seinfeld, J. H. and Pandis, S. N.: Atmospheric Chemistry and Physics: From Air Pollution to Climate Change, 3rd ed., Wiley, 2016.

Simpson, W. R., Mao, J., Fochesatto, G. J., Law, K. S., DeCarlo, P. F., Schmale, J., Pratt, K. A., Arnold, S. R., Stutz, J., Dibb, J. E., Creamean, J. M., Weber, R. J., Williams, B. J., Alexander, B., Hu, L., Yokelson, R. J., Shiraiwa, M., Decesari, S., Anastasio, C., D'Anna, B., Gilliam, R. C., Nenes, A., St. Clair, J. M., Trost, B., Flynn, J. H., Savarino, J.,
775 Conner, L. D., Kettle, N., Heeringa, K. M., Albertin, S., Baccarini, A., Barret, B., Battaglia, M. A., Bekki, S., Brado, T. J., Brett, N., Brus, D., Campbell, J. R., Cesler-Maloney, M., Cooperdock, S., Cysneiros de Carvalho, K., Delbarre, H., DeMott, P. J., Dennehy, C. J. S., Dieudonné, E., Dingilian, K. K., Donateo, A., Doulgeris, K. M., Edwards, K. C., Fahey, K., Fang, T., Guo, F., Heinlein, L. M. D., Holen, A. L., Huff, D., Ijaz, A., Johnson, S., Kapur, S., Ketcherside, D. T., Levin, E., Lill, E., Moon, A. R., Onishi, T., Pappaccogli, G., Perkins, R., Pohorsky, R., Raut, J.-C., Ravetta, F.,
780 Roberts, T., Robinson, E. S., Scoto, F., Selimovic, V., Sunday, M. O., Temime-Roussel, B., Tian, X., Wu, J., and Yang, Y.: Overview of the Alaskan Layered Pollution and Chemical Analysis (ALPACA) Field Experiment, ACS ES&T Air, 1, 200–222, https://doi.org/10.1021/acsestair.3c00076, 2024.

Smith, J. D., Kinney, H., and Anastasio, C.: Aqueous benzene-diols react with an organic triplet excited state and hydroxyl radical to form secondary organic aerosol, Physical Chemistry Chemical Physics, 17, 10227–10237,
785 https://doi.org/10.1039/c4cp06095d, 2015.

Smith, J. D., Kinney, H., and Anastasio, C.: Phenolic carbonyls undergo rapid aqueous photodegradation to form low-volatility, light-absorbing products, Atmos Environ, 126, 36–44, https://doi.org/10.1016/j.atmosenv.2015.11.035, 2016.

Song, H., Lu, K., Ye, C., Dong, H., Li, S., Chen, S., Wu, Z., Zheng, M., Zeng, L., Hu, M., and Zhang, Y.: A comprehensive observation-based multiphase chemical model analysis of sulfur dioxide oxidations in both summer and winter, Atmos
790 Chem Phys, 21, 13713–13727, https://doi.org/10.5194/acp-21-13713-2021, 2021.

Sunday, M. O., Heinlein, L. M. D., He, J., Moon, A., Kapur, S., Fang, T., Edwards, K. C., Guo, F., Dibb, J., Flynn III, J. H., Alexander, B., Shiraiwa, M., and Anastasio, C.: Hydrogen Peroxide Photoformation in Particulate Matter and its Contribution to S(IV) Oxidation During Winter in Fairbanks, Alaska, https://doi.org/10.5194/egusphere-2024-3272, 29 October 2024.

795 Tilgner, A., Schaefer, T., Alexander, B., Barth, M., Collett, J. L., Fahey, K. M., Nenes, A., Pye, H. O. T., Herrmann, H., and McNeill, V. F.: Acidity and the multiphase chemistry of atmospheric aqueous particles and clouds, Atmos Chem Phys, 21, 13483–13536, https://doi.org/10.5194/acp-21-13483-2021, 2021.

Wander, R., Neta, P., Dorfman, L. M., Flory, P. J., and Dorfman, L. M.: Pulse Radiolysis Studies. XII. Kinetics and Spectra of the Cyclohexadienyl Radicals in Aqueous Benzoic Acid Solution, Journal of Physical Chemistry, 72, 2946–2949, https://doi.org/https://doi.org/10.1021/j100854a044, 1968.

Wang, X., Gemayel, R., Hayeck, N., Perrier, S., Charbonnel, N., Xu, C., Chen, H., Zhu, C., Zhang, L., Wang, L., Nizkorodov, S. A., Wang, X., Wang, Z., Wang, T., Mellouki, A., Riva, M., Chen, J., and George, C.: Atmospheric Photosensitization: A New Pathway for Sulfate Formation, Environ Sci Technol, 54, 3114–3120, https://doi.org/10.1021/acs.est.9b06347, 2020.

Wenk, J. and Canonica, S.: Phenolic antioxidants inhibit the triplet-induced transformation of anilines and sulfonamide antibiotics in aqueous solution, Environ Sci Technol, 46, 5455–5462, https://doi.org/10.1021/es300485u, 2012.

Ye, C., Liu, P., Ma, Z., Xue, C., Zhang, C., Zhang, Y., Liu, J., Liu, C., Sun, X., and Mu, Y.: High H_2O_2 Concentrations Observed during Haze Periods during the Winter in Beijing: Importance of H_2O_2 Oxidation in Sulfate Formation, Environ Sci Technol Lett, 5, 757–763, https://doi.org/10.1021/acs.estlett.8b00579, 2018.

Yu, C., Liu, T., Ge, D., Nie, W., Chi, X., and Ding, A.: Ionic Strength Enhances the Multiphase Oxidation Rate of Sulfur Dioxide by Ozone in Aqueous Aerosols: Implications for Sulfate Production in the Marine Atmosphere, Environ Sci Technol, 57, 6609–6615, https://doi.org/10.1021/acs.est.3c00212, 2023.

Zhou, R., Liu, J., Zhou, C., and Zhang, X.: Phototransformation of Lignin-related Compounds in Chromophoric Dissolved Organic Matter Solutions, Water Res, 245, https://doi.org/10.1016/j.watres.2023.120586, 2023.